Charles University in Prague
Faculty of Mathematics and Physics

DIPLOMA THESIS

Marika Kubová

Optical Properties of Scintillators

Institute of Physics of Charles University

Supervisor of Diploma Thesis: Doc. RNDr. Miroslav Kučera, CSc.
Study program: Physics, Optics and Optoelectronics

2007

Univerzita Karlova v Praze
Matematicko-fyzikální fakulta

DIPLOMOVÁ PRÁCE

Marika Kubová

Optické vlastnosti scintilačních materiálů

Fyzikální ústav Univerzity Karlovy

Vedoucí diplomové práce: Doc. RNDr. Miroslav Kučera, CSc.
Studijní program: Fyzika, Optika a optoelektronika

2007

First, I would like to thank my family that they supported me. I am very grateful to the supervisor of my Diploma Thesis Doc. RNDr. Miroslav Kučera, CSc. for his valuable advice, support and patience. I also wish to thank Ing. Karel Nitsch, CSc. for preparing the samples. My thanks also belong to Ing. Martin Nikl, CSs., Dr. Natalja Solovieva, and Ing. Jan Pejchal for useful discussions and consultations. Special thanks belong to David Schmoranzer and my sister Radana Kubová for proofreading the manuscript.

I hereby declare, that I have written my Diploma Thesis by myself using the cited references exclusively. I give my approval concerning lending and publishing this Thesis.

Prague Marika Kubová

Contents

Chapter 1

Introduction

Scintillator materials are converters transforming high energy photons (X-, γ-rays) or energy of other particles into a number of photons from the UV/visible spectral range, which can be detected easily by conventional photodetectors, such as photomultipliers, photodiodes, or CCD detectors. Wide-gap single crystal scintillators found applications in many fields of human activity, e.g. in industrial defectoscopy, modern medical imaging methods, security systems, detectors in high energy and nuclear physics, etc. [1]-[6]. Some applications using X-rays or accelerated electrons require detectors of high 2D-spatial resolution. These detectors are often based on very thin plates (about a few μm) of Ce doped yttrium aluminum garnet (Ce:YAG) due to its fast scintillation response, high efficiency and favorable mechanical and chemical properties of this material. To increase the density and stopping power of this material, Y^{3+} ions can be replaced by heavier Lu^{3+} ions in the garnet structure.

High preparation temperature of Ce:YAG and Ce:LuAG single crystals grown by the Czochralski method (about 2000°C) results in the presence of a variety of point defects, such as antisite defects, vacancies, etc. [7], [8]. These defects can degrade light yield and timing characteristics of scintillator materials. Spatial resolution of the scintillator detector is limited by the thickness of the material. It is not possible to cut single crystals in plates of thickness about a few μm. An interesting alternative is offered by the preparation of thin films using the liquid phase epitaxy (LPE) method. It provides high quality single crystal layers at much lower growth temperatures (about 1000°C). Hence, they contain a smaller amount of intrinsic crystal defects. The disadvantage of this method is that some residual concentration of the flux compound can be incorporated into the films. This is a typical feature of the $PbO - B_2O_3$ flux. As a novelty, LPE growth of Ce:YAG and Ce:LuAG from $BaO - BaF_2 - B_2O_3$ flux will be attempted.

The aim of this work is to compare optical, emission, kinetic, and crystallographic properties of Ce:YAG epitaxial layers prepared from PbO-based and BaO-based fluxes and to look for ideal growth conditions. The main text of this Diploma Thesis consists of six Chapters. Chapter 2 summarizes general physical principles of luminescence of localized luminescent centres in the crystal lattice. Chapter 3 introduces the concept of a scintillator, lists key scintillator characteristics, and mentions the most important applications in which scintillator detectors are used. Material properties of studied materials are described in Chapter 4. In Chapter 5, the technological process of preparation of thin films by the LPE method is explained, applied melt composition and detailed information about epitaxial films are described as well. Chapter 6 provides technical details of the experimental setup in which optical spectra and kinetics of luminescence were measured. Chapters 7 presents the experimental results and their discussion. Chapter 8 contains a conclusion of the summarized results.

Chapter 2

Luminescence

2.1 Introduction to luminescence

Luminescence is the radiative emission process, in which an atomic system returns to its ground state by spontaneous emission of photons. In general, luminescence is the emission of light from a system that is excited by some form of energy. According to excitation energy we have various types of luminescence listed in Table 2.1.

Name	Excitation mechanism
Photoluminescence	Light
Cathodoluminescence	Electrons
Radioluminescence	X-rays, α-, β-, γ-rays
Thermoluminescence	Heating
Electroluminescence	Electric field or electrical current
Triboluminescence	Mechanical energy
Sonoluminescence	Sound waves in liquids
Chemiluminescence and Bioluminescence	Chemical reactions

Table 2.1: Various types of luminescence according to excitation energy, Solé et al. [9].

Luminescence in solids can have two origins: intrinsic and extrinsic. Luminescence may originate in ideal pure crystal lattice (intrinsic) or on lattice defects or impurities, so called impurity luminescent centres (extrinsic). Crystal lattice acts as a transport medium in which the luminescent centres are fixed. Then it collects excitation energy and transfers it effectively to the luminescent centres. Changes in structure of electron energy levels of centres may occur due to interaction of electron shells of impurity centres with the lattice. Thereby their optical spectra can be modified. In the special case of electroluminescence, crystal lattice ensures electric conductivity for the excitation of centres. A factor responsible for the influence of the host lattice on the optical properties of a given ion is the crystal field. This is the electric field at the site of the ion under consideration due to the surrounding ions. A positive ion doped into a crystal finds itself surrounded by anions. These negative ions produce an electric field which perturbs the atomic levels of the ion. The spectral position of certain optical transitions is determined by the strength of the crystal field. Additionally, the crystal field lifts degeneracies of energy levels. The levels are split because in the host not all directions are

equivalent. This is determined by the symmetry of the crystal lattice. Different host lattices lead to different crystal fields and therefore to different splittings. In this way the optical centre can serve as a probe of its surroundings. Observed splittings show the symmetry of the site.

2.2 Stokes shift of luminescent spectra

Absorption and emission spectra do not peak at the same energy. The emission spectrum is shifted to lower energies relative to the absorption spectrum. This shift is called Stokes shift. Let us consider an optical ion with two levels in a crystal. Ions in solids are vibrating around their equilibrium positions. An ion sees its neighbours in different positions. Hence, each state has to be considered as a continuum of states. Ions follow harmonic motion. These two energy levels become parabolas according to the potential energy of the harmonic oscillator model.

In general, the equilibrium positions of the ground and excited states can be different ($\Delta R \neq 0$). The electronic transition occurs in four steps, as shown in Fig. 2.1. First, an electron is promoted from the minimum of the ground state to the excited state without change in distance coordinate. Afterwards, the electron relaxes within the electron state nonradiatively by emission of phonons. From the minimum of the excited state the electron comes to the ground state and a luminescent photon is emitted. Finally, the electron relaxes to the minimum of the ground state. As a result the emission occurs at a frequency which is lower than the frequency of absorption.

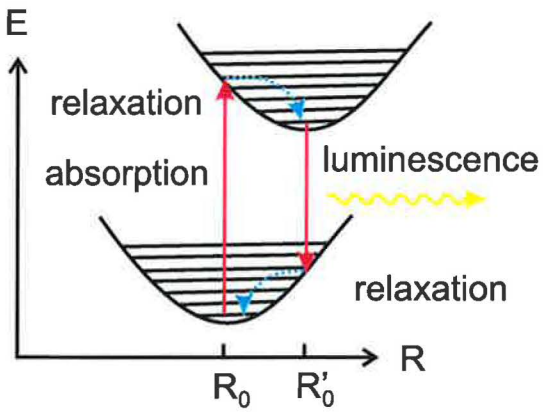

Figure 2.1: Configuration diagram for the ground state and the excited state of an impurity centre. R is the internuclear distance. The optical transitions are indicated by the vertical arrows. The parabola offset is $\Delta R = R'_0 - R_0$. Absorption and emission shows Stokes shift.

The optical transitions in Fig. 2.1 are sketched by a vertical arrows. Since R is the internuclear distance and the electrons move much faster than the nuclei. The electronic transitions between ground state and excited state take place in static surroundings, in good approximation.

If the two parabolas lay exactly one above another, the absorption band would become a narrow line. This is the case of trivalent rare earth ions, e.g. Eu^{3+} ions in Y_2O_3 host lattice. The $4f$ orbital of Eu^{3+} lies inside the ion and is shielded from the surroundings by the filled $5s^2$ and $5p^6$ orbitals. Therefore, the influence of the host lattice on the optical transitions

within the $4f^n$ configuration is small and the parabola offset is $\Delta R \approx 0$. $4f \rightarrow 4f$ transitions are strongly forbidden by the parity selection rule. Hence they are much weaker than the allowed transitions, Blasse and Grabmaier [10].

The allowed $4f \rightarrow 5d$ optical transitions have $\Delta R \neq 0$ and appear in the absorption spectra as intense broad bands. The larger the value of ΔR, the broader the absorption band.

The intensity of the optical absorption transition is influenced thereby, if the transitions between ground and excited states are allowed or forbidden. This is governed by selection rules. First important is the spin selection rule which forbids electronic transitions between levels with different spin ($\Delta S \neq 0$). The parity selection rule is significant as well, it forbids electric-dipole transitions between levels with the same parity, for example electronic transitions within the d shell, within the f shell, or between the d and the s shells. These selection rules are not absolute rules in solids. Since some relaxation of selection rules can occur due to spin-orbit coupling, electron-vibration coupling and uneven crystal field components.

2.3 Kinetics of luminescence

The excited luminescent centre is found in thermodynamic nonequilibrium state and after certain time it loses its excitation energy and returns to the ground state by radiative, light-emitting and nonradiative processes which are characterized by radiative lifetime τ_r and nonradiative lifetime τ_{nr}, respectively. The total transition rate is given as follows:

$$\frac{1}{\tau} = \frac{1}{\tau_r} + \frac{1}{\tau_{nr}}. \tag{2.1}$$

The quantum efficiency of luminescence is the ratio of the radiative emission probability to the total deexcitation probability

$$\eta = \frac{1/\tau_r}{1/\tau_r + 1/\tau_{nr}} = \frac{\tau}{\tau_r} = (\leq 1). \tag{2.2}$$

Let us consider localized impurity luminescent centre in a crystal lattice. The centre absorbs energy and is promoted to the excited state. The concentration of excited centers is lowered due to radiative and nonradiative transitions, see Fig. 2.2. The time evolution of the excited state population follows differential equation:

$$\frac{dn}{dt} = -\frac{n}{\tau_r} - \frac{n}{\tau_{nr}} = -\frac{n}{\tau}, \tag{2.3}$$

where n is the concentration of centres in excited state. The solution of the differential equation 2.3 gives

$$n(t) = n(0) \cdot e^{-\frac{t}{\tau}}, \tag{2.4}$$

where $n(0)$ is the concentration of excited centres at $t = 0$ after the absorption of a light pulse. The intensity of emitted light is given as the concentration of centres in excited state which return to the ground state by radiative transition:

$$i(t) = \frac{n(t)}{\tau_r} = i(0) \cdot e^{-\frac{t}{\tau}}, \tag{2.5}$$

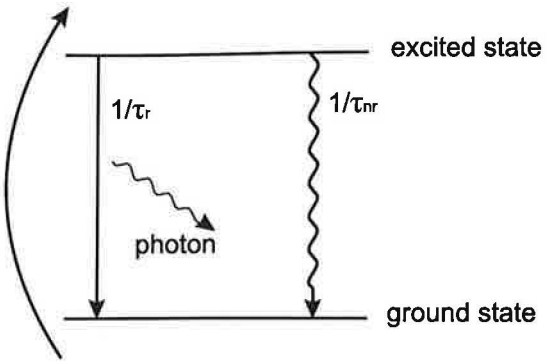

Figure 2.2: Time evolution of the excited state population. Luminescent centres are promoted to the excited state by absorption of energy and can return to the ground state radiatively or nonradiatively, Nikl [1].

where $i(0)$ is the intensity at $t = 0$ and τ is the decay time of luminescence and it characterizes the decrease in excited state population due to radiative and nonradiative transitions simultaneously and can be determined experimentally. As a result, a one-exponential decay of luminescence intensity was obtained. Presence of two kinds of localized luminescent centres shows two-exponential decay:

$$i(t) = a_1 \cdot e^{-\frac{t}{\tau_1}} + a_2 \cdot e^{-\frac{t}{\tau_2}}, \tag{2.6}$$

where a_1, a_2 are amplitudes and τ_1, τ_2 are decay times of luminescence of the first and second component, respectively.

2.4 Luminescent centres

Defects and impurities can act as luminescent centres in crystalline host materials. Pure colourless crystals doped by optically active impurities acquire strong colours, as is the case of ruby, Fox [11]. Sapphire itself is transparent. The characteristic red colour of ruby arises from the optical transitions of chromium impurities. Paramagnetic ion impurities in ionic crystals can act as luminescent centres. These materials are widely used in solid state lasers and phosphors for fluorescent lighting and cathode ray tubes. The impurities will normally be present at a low density, so that the interactions between neighbouring dopants are negligible due to their large separation. The perturbation of the electronic levels of the dopant ions due to the crystalline environment, in which they are placed, is the main effect. The optical properties of free ions in the gas phase are characterized by sharp emission and absorption lines. When the same ions are incorporated into a crystalline host, the optical properties will be modified by the interaction with the crystal. The properties of the $3d$ and $4f$ series of paramagnetic ions are different.

Rare earth ions have the electronic configuration $4f^n 5s^2 5p^6$, the outer $6s$ electrons are removed. The magnitude of the crystal field effect is relatively small due to the screening of the optically active $4f$ levels with the filled $5s$ and $5p$ shells. The emission and absorption spectra will remain as discrete lines. Spin-orbit coupling has a much larger influence. It varies as Z^4, Z is the atomic number, and in this case it is in the range 58-70. The spin-orbit interaction splits the $4f$ levels. The crystal field then perturbs these states, shifting their

energies slightly and causing new small splittings of levels that are degenerate in the free ions.

Transition metal ions have the electronic configuration $3d^n$ ($4s$ electrons are removed). They interact strongly with the crystal field. This is due to the relatively large radius of the $3d$ orbitals and the fact that they are unshielded by outer filled shells. Hence they are very sensitive to the crystalline environment. The crystal field effect is much stronger than spin-orbit interaction, they have Z in the range 21-30. The absorption and emission spectra consist of continuous bands and show the Stokes shift. This is a consequence of strong vibronic broadening of the ground state and the excited states. These ions are useful for making tunable lasers.

Chapter 3

Scintillators

3.1 The principle of a scintillator

Scintillator materials transform high energy photons into the photons from the visible spectral range, which can be registered using common photodetectors, such as photomultipliers, photodiodes and CCD detectors, as shown in Fig. 3.1. There exists a large amount of published information on this topic [1]-[4], [10], [12] and references therein. Scintillation conversion is a relatively complicated issue, which can be divided into three consecutive sub-processes: conversion, transport and luminescence, see Fig. 3.2.

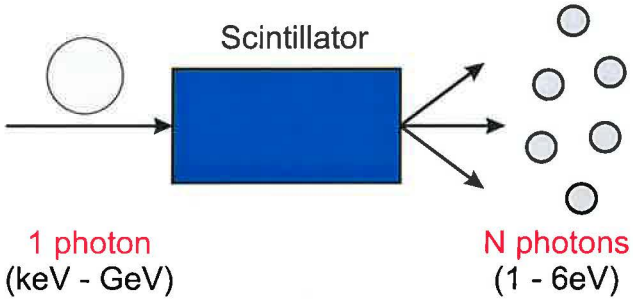

Figure 3.1: Sketch of the principle of a scintillation detector. Scintillator material converts a high energy photon into photons from visible spectral range, Nikl [1].

Conversion

A multi-step interaction of a high energy photon with the lattice of the scintillator material occurs through the photoelectric effect and Compton scattering. Many electron-hole pairs are created and thermalized in the conduction and valence bands. This first stage is concluded within less than 1 ps.

Transport

Electrons and holes migrate through the material. They may be repeatedly trapped at defects. Energy losses are possible due to nonradiative recombination. Considerable delay can occur due to the charge carrier recapture at trapping levels in the material band gap. Point defects, flaws in the material and surfaces can introduce energy levels into the band gap and degrade otherwise high intrinsic scintillation performance.

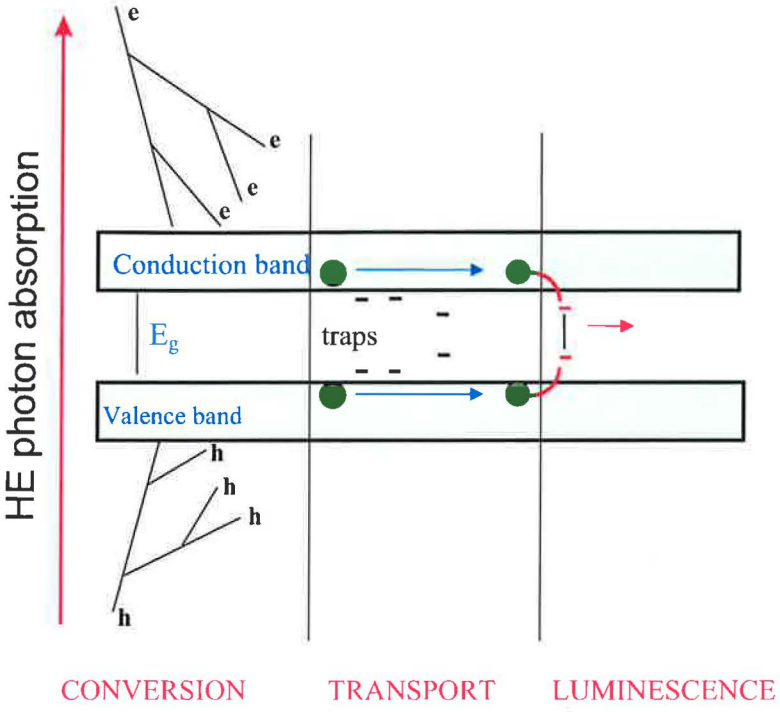

Figure 3.2: Scintillator conversion menchanism. The process is divided into three consecutive stages of coversion, transport and luminescence described in the text, Nikl [2].

Luminescence

Luminescence consists in consecutive trapping of the electron and hole at the luminescent centres and their radiative recombination.

3.2 Characteristics and paramenters of scintillator materials

There is considerable interest in finding a scintillator material with optimal scintillation properties. The most important characteristics are:

Light yield: is a number of generated visible photons which arrive at the photodetector within a certain time (e.g. 1 μs) after the high-energy photon absorption (1 MeV).

X-ray stopping power: depends on the thickness of the material, on its density, ρ, and on its effective atomic number, Z_{eff}. The effective atomic number is a term that is similar to atomic number but is used for compounds and mixtures of different materials rather than for atoms, defined in [12]. It is calculated by taking the fractional proportion of each atom in the compound and multiplying that by the atomic number of that atom. Absorption by photoelectric effect per cm is proportional to $\propto \rho Z_{eff}^4$, Zorenko [13].

Scintillation response – decay time: is given by the characteristics of the transport and luminescence stages as they are slower with respect to the initial conversion, in transitions of Ce^{3+} tens of ns.

Other significant parameters are:

Spectral matching between the scintillator emission spectrum and photodetector spectral sensitivity: The emission spectrum of the scintillator should peak near the maximum quantum efficiency of the photodetector. For the photomultiplier, the near UV-blue emission is optimum. For the photodiode and the CCD, the green-red spectral region was considered the most appropriate.

Chemical stability: mainly the hygroscopicity of materials which in some cases severely limits their long-time operation in the open air.

Radiation resistance: The changes and instabilities in the material due to irradiation. In case that the induced absorption overlaps with the emission spectrum, re-absorption losses occur and result in a loss in the light yield.

Energy resolution: Ability to distinguish two energetically close photons.

Cost: The growth technique, the cost of material and the required purity of material are important parameters. Especially in applications in which large volumes of scintillator material are needed, for example the Large Hadron Collider in Cern.

For more information see Nikl [1], [3] and Rodnyi [12] and references therein.

There is no material which would meet all of these criteria perfectly. The choice of a suitable scintillator is always a compromise among the above factors according to the requirements of particular applications.

3.3 Applications

The research of scintillator materials began in the 19th century after the discovery of X-rays. At the end of the 19th century, energetic photon and particle radiation was available and its enormous application potential forced strongly the development of scintillator materials to be used in their exploitation. The single crystals with wide band-gap, oxides, and halogenides are mostly used, because of their quality. Each defect can lower the luminescence efficiency of the scintillator materials. In the last twenty years, the development of these materials was accelerated due to the rising amount of their practical applications.

A high-quality scintillator that meets the basic requirements of both a fast response and a high light yield is hard to find, Fig. 3.3. Materials such as NaI:Tl, CsI:Tl, CsI:Na, BGO, and $CdWO_4$ have light yields of $\geq 10^4$ photons/MeV but decay times >200 ns. On the other hand, BaF_2, CsF, CeF_3, and CsI, which have decay times in the range of ~1-30 ns, have light yields of only a few thousand photons per MeV for the fast components. There are essentially four mechanisms for fast scintillators: core-valence luminescence (very fast response time (~1 ns) but low light yield, application in neutron detection), CsI (fast response but low light yield), $PbWO_4$ (fast response due to luminescence quenching but low light yield, application in high-energy physics), and allowed $5d$ - $4f$ transitions in lanthanide ions, which is the most

Table 1
Commercially available inorganic scintillators, data at RT[a]

	NaI:Tl	CsI:Tl	CsI:Na	BGO	$CdWO_4$	BaF_2	CsF	CeF_3	CsI	GSO:Ce	YAP:Ce	^{6}Li glass:Ce	^{6}LiF/ZnS:Ag	^{6}LiI:Eu
Emission max., nm														
Slow	410	565, 420	420	480	500	310			450				450	470
Fast						220	390	285, 305	320	440	350	400		
Light yield, gammas Photons/MeV, slow	4.1×10^4	6.6×10^4	4.0×10^4	0.9×10^4	2.8×10^4	1.1×10^4			200	1000			7.5×10^4	1.2×10^4
Fast						1500	2000	~4000	2000	8000	2.1×10^4	~4000		
Light yield, Photons/neutron												~6000	16×10^4	5.0×10^4
Decay time, slow, μs	0.23	0.8->6	0.63	0.30	~3/~17	0.60			1.0	0.6			~1	1.4
Fast, ns						0.8	2.9	5/31	~6/~28	60	30	75		
Refractive index	1.85	1.80	1.84	2.15	2.2	1.50	1.48	1.62	1.95	1.85	1.93	1.56	2.36	1.96
Density, g/cm^3	3.67	4.51	4.51	7.13	7.9	4.88	4.11	6.16	4.51	6.71	5.5	2.5-2.7	4.1	4.1
ρZ^4_{eff}, 10^6	24.5	38	38	227	134	38	33	50	38	84	7			31
Radiation length, cm	2.6	1.8	1.8	1.1	1.1	2.0	2.0	1.7	1.8	1.4	2.9			
ΔE/E(662 keV), FWHM, %	5.6	4.3	7.4	9.0	6.8	7.7				7.8	4.4			
Hygroscopicity	Yes	Slightly	Yes	No	No	No	Very	No	Slightly	No	No	No	No	Very
References	[3–8]	[6,7,9–12]	[6,7,13–15]	[4,6,7,16–19]	[6–8,20,21]	[22–26]	[27–31]	[32–34]	[10,35–38]	[6,39–42]	[43–46]	[47–51]	[48,52]	[53–55]

[a] BGO = $Bi_4Ge_3O_{12}$, GSO = Gd_2SiO_5, YAP = $YAlO_3$
[6] Li glass, e.g. GS20 = $(SiO_2)_{0.56}(MgO)_{0.04}(Al_2O_3)_{0.18}(^6Li_2O)_{0.18}(Ce_2O_3)_{0.04}$ [47].

Figure 3.3: Commercially available inorganic scintillators, data at room temperature, [14].

promising mechanism, because of its response time of 10-100 ns and light yield >20 000 photons/MeV of absorbed radiation energy. From lanthanide ions, Ce^{3+} incorporated into some host material is very efficient, with short decay time and its emission spectrum matches well with photodetector spectral sensitivity.

The scintillation detectors consist of a scintillator material followed by a photodetector, such as photodiode, photomultiplier or CCD detector. Scintillation detectors are used to register X-rays or gamma rays. From the large number of applications using X-rays across many fields of human activity - flaw detection, high energy physics (Large Hadron Collider in Cern, $PbWO_4$), geology, radio (X-ray) astronomy - special interest will be devoted to medical imaging and high resolution 2D imaging. The total consumption of scintillator materials is 120 tons per year, which is the same amount applied in LHC in Cern.

Medical imaging

Photographic film is being replaced by modern flat panel detectors, Fig. 3.4. An array of amorphous silicon photodiodes positioned on a glass plate is covered by a scintillator screen of columnar grown CsI:Tl. With respect to classical film the modern flat panel detector offers better sensitivity at the same 2D resolution, all-electronic image processing, improved image quality, easier and faster data processing, reduced operation costs and lower irradiation doses for the patients. Scintillator materials $YAlO_3$: Ce, $Bi_4Ge_3O_{12}$ are applied for example in general radiography, dental imaging, mammography, and computer tomography (CT).

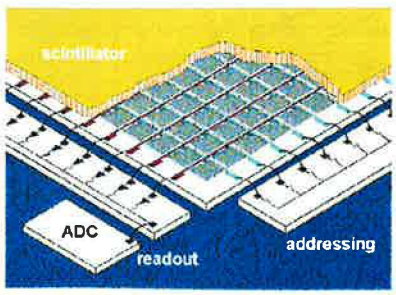

Figure 3.4: Schematic of a flat-panel detector for medical imaging, [3].

Scintillators in medicine must have: high light yield, fast scintillation response, high density, and high spatial resolution.

Positron emission tomography

Positron emission tomography utilizes annihilation of a positron with an electron. As a result, two photons with the energy 511 keV are generated. They scatter to the opposite directions at the same line and are registered by a circular detector around the patients head. From the points of intersection of these lines we can obtain a 3D image of the nerve centres in the human brain with a resolution of 2 mm. The principle is sketched in Fig. 3.5.

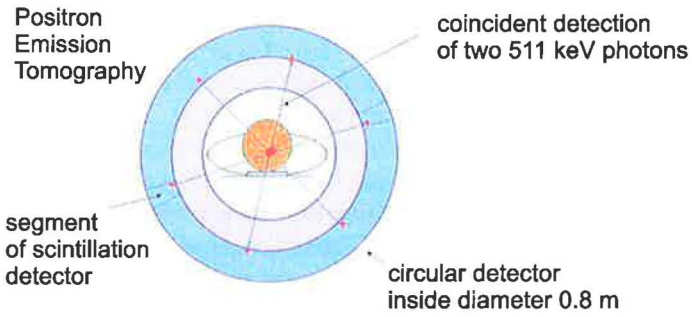

Figure 3.5: Scheme and principle of the positron emission tomography, [1]

Imaging screens

Imaging screens with high spatial resolution of about 10 μm are used to detect soft X-ray or low energy electron beams. About 5 μm thick Ce:YAG scintillator plate is glued onto a fibre optical plate and attached to a CCD sensor, Fig. 3.6. Spatial extent of the light cone is given by the thickness of the scintillator plate and by total light reflection. This is why plates have to be as thin as possible. They are prepared in the form of thin films. However, the stopping power of the scintillator is limited due to its thickness. Therefore, we need scintillator materials with high density. To increase density it is possible to replace yttrium by lutetium. In this application Ce:YAG or Ce:LuAG are commonly used. This work is dealing with these materials.

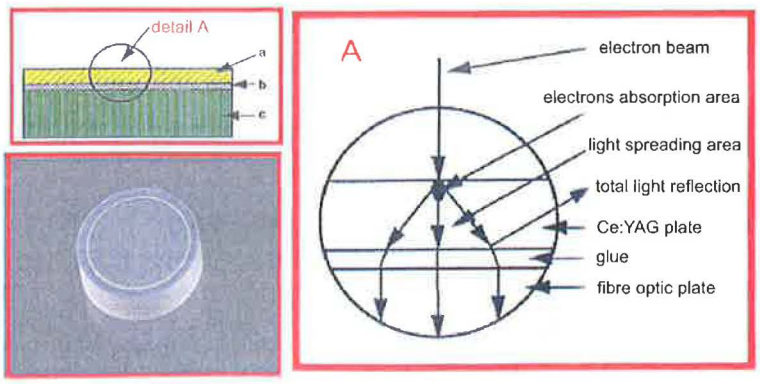

Figure 3.6: Sketch of a high 2D resolution X-ray or electron beam sensor and the photograph of the sensor head, **a** Ce:YAG plate (5-50 μm), **b** glue, **c** fiber optical plate. In the detail **A**, it is shown how resolution is limited due to thickness, [3]

Chapter 4

Material properties of Ce:YAG and Ce:LuAG

YAG and LuAG are abbreviations of yttrium aluminum garnet and lutetium aluminum garnet, respectively. Doped by cerium they are fast scintillators with excellent mechanical and chemical resistance and can be cut into a variety of shapes and sizes. Both materials have short decay time ~60 ns. This is the advantage in time dependent and coincidence measurements. The maximum of the emission is in green-yellow spectral range, which matches very well with photodetector spectral sensitivity. There are a lots of applications using Ce:YAG and Ce:LuAG: positron emission tomography (PET) scanners, high energy gamma and charged particle detection, and high spatial resolution imaging screens for gamma, X, beta and UV rays, Section 3.3. A particular advantage of Ce:LuAG is its higher density and effective atomic number resulting in thinner screens with higher spatial resolution, Table 4.1.

Unfortunately, the scintillation performance of these material can be degraded by the occurrence of antisite defects such as Lu_{Al}, Y_{Al}. Such defects arise in the material structure sketched in Fig. 4.1 as a result of the occurrence of Lu^{3+}, or Y^{3+} ions at the Al^{3+} octahedral sites. This defect constitutes a shallow electron trap, which delays energy delivery to the Ce^{3+} emission centers due to retrapping charge carriers migrating around. It slows down the scintillation response of the material. Thermoluminescence measurements appear as a sensitive diagnostic tool to evidence these defects in the single crystals grown by the Czochralski method, Nikl et al. [7], Vedda et al. [8]. Antisite defects are present in both YAG and LuAG garnets. But in LuAG host, their concentration is higher as a result of higher growth temperature and smaller misfit between the Lu^{3+} and Al^{3+} ionic radii.

4.1 Garnet structure

Garnet has a cubic structure, space group O_h^{10}, with an elementary cell containing 8 molecules (160 atoms, 96 oxygen ions and 64 cations). Cations may occupy three different positions: dodecahedral (c, {}), octahedral (a, []), and tetrahedral (d, ()), see Fig. 4.2. A typical chemical formula of garnet is $\{A_3\}[B_2](C_3)O_{12}$ with three kinds of cations in three types of positions. Each cation is placed in the centre of the polyhedron surrounded by O^{2-} ions in its corners. Coordination polyhedrons are illustrated in Fig. 4.3.

In the yttrium aluminum garnet, Y^{3+} ions occupy dodecahedral positions, Al^{3+} fill octahedral and tetrahedral positions. The important factor is the size of the ions. In the centre of the dodecahedron there is much more space for ions with larger radius such as Y (ionic

Physical properties	YAG	LuAG
chemical formula	$Y_3Al_5O_{12}$	$Lu_3Al_5O_{12}$
crystal scructure	cubic	cubic
molecular mass M [g/mol]	594	852
lattice constant a_0 [Å]	12.00	11.92
melting point T_m [°C]	1970	2050
density ρ [kg/m^3]	4.56	6.67
effective atomic number Z_{eff}	29	58.9
Scintillation properties	**Ce:YAG**	**Ce:LuAG**
Light yield [photon/MeV]	24000	12500
Decay time τ [ns]	62	54
Emission maximum λ [nm]	550	530

Table 4.1: Material properties of YAG and LuAG, [3], [13], [16], [17].

radius 1.06 Å, [15]), or RE^{3+} (=rare earth) ions. However, in the tetrahedron there is not enough space for them. Hence, these sites are filled with small ions, such as Al ions (ionic radius 0.57 Å, [15]), Ga, etc. The chemical formula can be written as $\{Y_3^{3+}\}[Al_2^{3+}](Al_3^{3+})O_{12}^{2-}$. When YAG lattice is doped with cerium, Ce^{3+} ions replace Y^{3+} ions at sites of D_2 symmetry in the dodecahedron made up of eight O^{2-} ions at its corners.

In lutetium aluminum garnet lutetium ions occupy the same position as yttrium ions in the garnet structure, that means in the centre of the dodecahedron, Fig. 4.1.

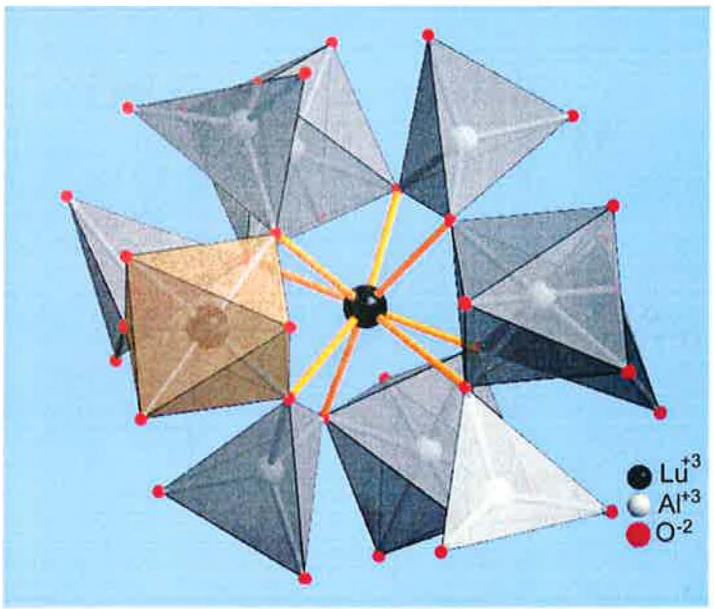

Figure 4.1: Structure of lutetium alluminum garnet. In the middle of the picture there is a Lu^{3+} ion in a dodecahedral site, black drawn. Al^{3+} ions fill positions in the centres of octahedrons and tetrahedrons. O^{2-} ions are placed in the corners of polyhedrons. Antisite defect Lu^{3+} ion at Al^{3+} site (Lu_{Al}) is sketched in the middle left octahedron, Nikl [7].

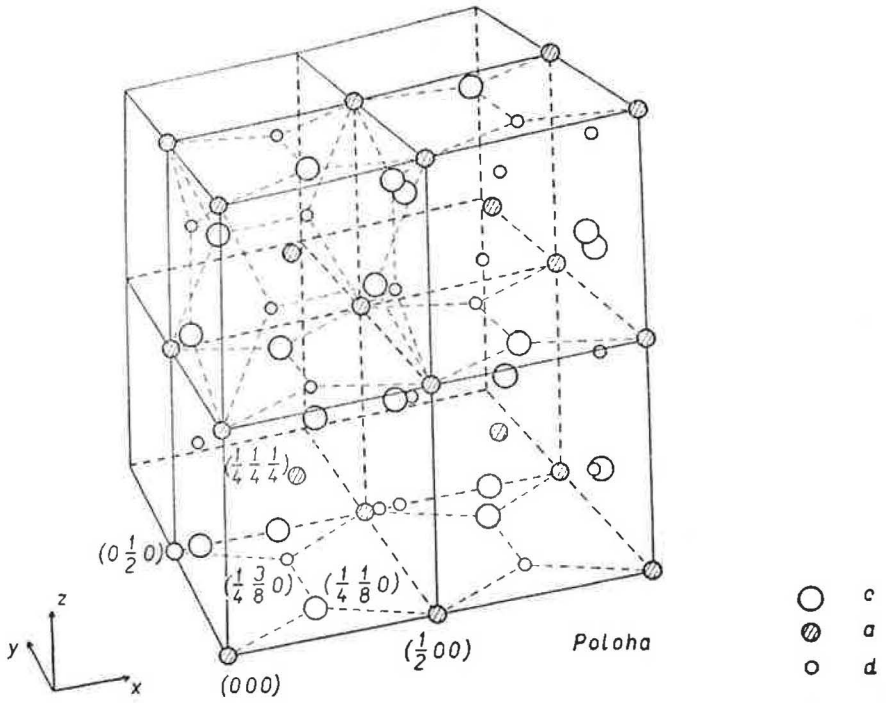

Figure 4.2: Positions of cations in garnets. **c** is dodecahedral, **a** octahedral and **d** tetrahedral position. Oxygen ions are not drawn, Krupička [15].

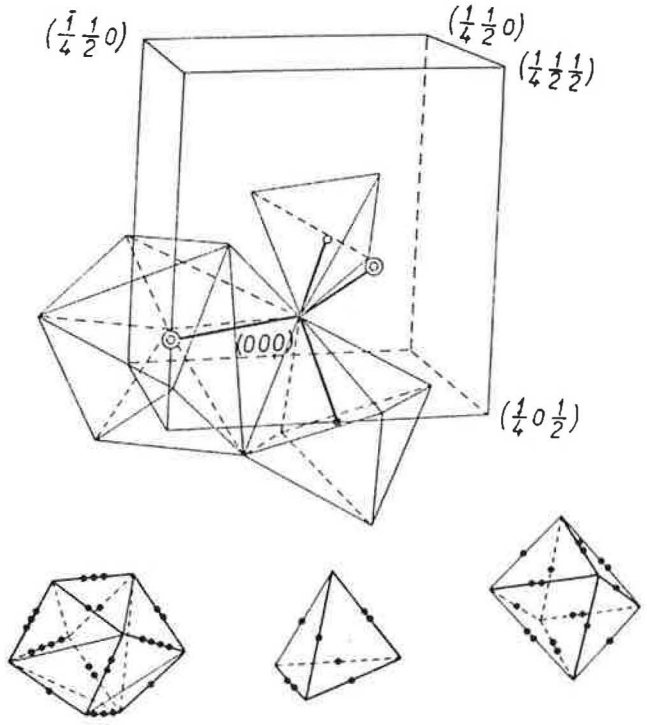

Figure 4.3: Coordination polyhedrons and their organization in the garnet structure, Krupička [15].

4.2 Energy levels

Ce:YAG has wide band gap of about 7 eV, Tomiki [18]. The valence band is created by $2p$ states of oxygen. The conduction band is made of $4d$ and $5s$ states of yttrium. Ce^{3+} ion has the electronic configuration $4f^1$. The ground term ^2F is split into two manifolds. The deeper level $^2F_{5/2}$ is occupied by an electron and the upper level $^2F_{7/2}$ is almost empty at room temperature. The distance between these two levels is about 0.21 eV. The excited state $5d^1$ of Ce^{3+} is split into five levels in the crystal field of D_2 symmetry. Three peaks at 458 nm, 340 nm, and 230 nm in absorption and excitation spectra correspond to transitions from the $^2F_{5/2}$ ground state to the excited states, see Fig. 4.4, Table 4.2. The upper three levels are too close to each other. Hence, they overlap and only one peak is observed at 230 nm, which can be divided into three Gaussian bands, Fig. 7.47. The electron excited into any of these upper levels eventually makes a photon-emitting transition from the lowest d-level to the two levels ^2F of the ground state. Therefore, the emission spectrum is a broad band extending over the spectral range form 470 nm to 700 nm, which is composed of two overlapping bands corresponding to two levels $^2F_{5/2}$, $^2F_{7/2}$.

	Absorption spectrum	Excitation spectrum
i	$E_{max,i}$ [eV]	$E_{max,i}$ [eV]
1	2.715	2.659
2	3.653	3.643
3	4.800	4.660
4	5.485	5.440
5	5.920	6.070

Table 4.2: Energy positions of the absorption and excitation peaks, according to Tomiki [19]. The corresponding peak positions should have the same value. The disagreement is given by accuracy in the experiment, [19].

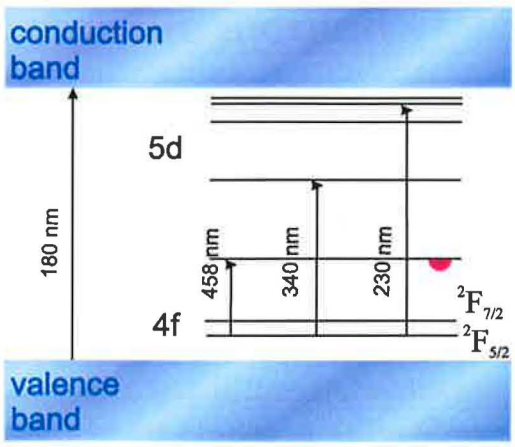

Figure 4.4: Scheme of energy levels in Ce:YAG. $5d$ levels are drawn as discrete levels for simplicity. In fact they create broad bands which are furthermore split due to the crystal field, Robbins [20]. Electrons excited into the upper levels relax very quickly. Luminescence occurs from the lowest level, marked with a red dot, and shows Stokes shift, Section 2.2.

Chapter 5

Liquid phase epitaxy

This Chapter focuses on the description of the preparation of samples. In a number of applications, very thin plates of scintillator materials are required. Especially in imaging screens the spatial resolution is limited due to the thickness of the material, Section 3.3. It is not possible to cut single crystals in plates of the thickness of about a few micrometers. It is better to prepare single crystal layers on transparent substrates.

The liquid phase epitaxy (LPE) method was developed for the growth of iron garnets for magnetic bubble memories. This technique enables to prepare high quality films with a very homogenous distribution of the activator ions and the reproducibility from sample to sample is very high. Therefore, this method was applied to preparation of non-magnetic garnets, Robertson et al. [21]. Flux added into the melt decreases the saturation temperature. At temperatures above the saturation temperature, the garnet is dissolved in the melt. Below the saturation temperature, crystallization occurs and the layer grows on the substrate.

Epitaxial layers prepared by LPE in comparison with their bulk equivalents grown by the Czochralski method provide low concentrations of intrinsic crystal defects and antisite defects, Zorenko et al. [22], [23], [24]. This is the result of much lower growth temperature in case of the LPE ($\sim$1000°C) in contrast with the Czochralski method ($\sim$1900°C).

5.1 The principle of the method

The design of the furnace used for the isothermal horizontal dipping liquid phase epitaxy for the growth of garnet films is shown in Fig. 5.1. The preparation of each sample follows these steps:

1. YAG single crystal grown by the Czochralski method was cut into 0.5 mm thick plates with a diameter of 20 mm. Then, the substrates were mechanically and chemically polished on both sides.

2. Film quality depends on defect free substrates without dust, dirt, or grease. That is why the substrate first has to be cleaned in warm sulphuric acid. Then it is fixed in the holder.

3. The melt of appropriate flux composition and the garnet placed in a platinum crucible inside the furnace is heated above its saturation temperature and mixed. This process takes quite a long time because the melt has to be completely homogenous.

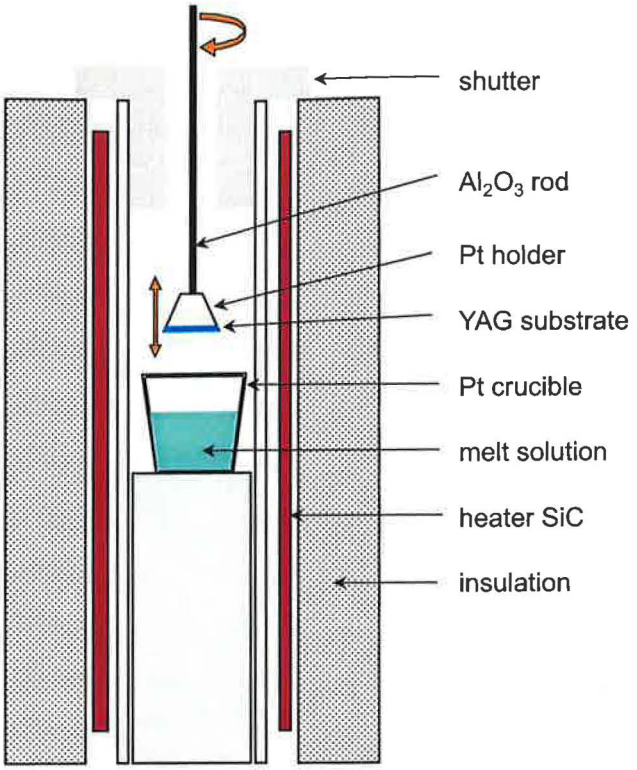

Figure 5.1: Schematic cross-section of the furnace for isothermal horizontal dipping liquid phase epitaxy.

4. Then the temperature is decreased to the growth temperature below the saturation temperature. The melt of applied composition, see Section 5.3, can be undercooled over tens of degrees, Winkler [25].

5. The substrate mounted in the holder is lowered slowly to the crucible with the melt solution. Equilibrium establishes. The substrate must have approximately the same temperature as the melt. Otherwise spontaneous crystallization may occur after immersion.

6. The substrate is dipped into the melt. The holder rotates about 160 rpm around its vertical axis to ensure uniform film growth.

7. The growth of the layer is isothermal and is not of the gradient transport type.

8. In the end of the growth process the substrate is withdrawn from the melt. The holder is rotated quickly at about 700 rpm to remove the residual melt from the surface of the crystal.

9. Finally, the substrate is slowly pulled out from the furnace to prevent cracking the film due to thermal shock. Afterwards, the surface of the crystal is cleaned mechanically and chemically - in warm nitric acid.

5.2 Factors affecting the luminescent efficiency of the epitaxial layer

Defect free substrates

The substrates must be free of dislocations, strains, inclusions, facets, dirt, or surface damage such as pits and scratches originating from the polishing procedure.

Lattice mismatch

The lattice mismatch between substrate and film must be less than the experimentally determined value of 0.016 Å, otherwise cracking or faceting of the film will occur due to strain. This leads to an increase of light output due to multiple reflection and surface scattering but also to a decrease of resolution, Robertson et al. [21]. Very thin epitaxial layers are flexible and resist greater differences in lattice constants. However, thick layers are much more sensitive to lattice mismatch.

Activator concentration

The light output of the scintillator material is a function of activator concentration in the layer. The Ce^{3+} ions in YAG show high cathodoluminescent efficiency at low concentration and the efficiency rises steeply with concentration of Ce in the layer, Robertson et al. [26]. This points at a good coupling of the cerium ion to the lattice and implies that it is a very efficient energy absorber.

The amount of activator ions included in a layer is characterized by the segregation coefficient. It is the ratio of concentration of a garnet constituent in the crystal to that in the melt. Knowledge of the segregation coefficient of each component is important for the calculation of the necessary flux composition. The number of Ce incorporated in YAG is much lower than of the other rare earths (Tb, Eu), because the cerium ion is larger. This leads to lower concentrations of Ce in YAG and therefore it is not possible to form a $Ce_3Al_5O_{12}$ garnet. When the CeO_2 concentration in the melt is raised, a second phase is created on the melt surface, [21].

Supercooling value ΔT

Supercooling is defined as

$$\Delta T = T_s - T_g, \tag{5.1}$$

where T_s is the saturation temperature of the melt and T_g is the growth temperature. The supercooling value in our experiment exceeds 2 to 52°C. The growth temperature must be controlled carefully, because the growth rate is approximately linear with the supercooling. The degree of supercooling should not be high. Otherwise, spontaneous nucleation may occur. This leads to destruction of the film or to modification of the composition of the melt if the spontaneous nucleation takes place outside the film, for example on the walls of the crucible.

The growth temperature is a very important parameter. The lower the growth temperature, the higher the concentration of impurities.

Melt composition

The purity of starting oxides influences strongly the luminescent efficiency, because some quench-ions may be included in the films. The melt consists of garnet constituents and the flux. For applied melt composition see Section 5.3.

5.3 Melt composition

The Ce doped $Y_3Al_5O_{12}$ was prepared using two types of flux: the PbO-based flux and the BaO-based flux. The garnet constituents are: Al_2O_3, Y_2O_3, CeO_2.

$PbO - B_2O_3$ flux

Epitaxial films grown from the PbO-based flux exhibit excellent crystallographic properties and a high quality surface. The disadvantage of the PbO-based flux is that it reacts with the platinum crucible. Platinum and lead ions are included in epitaxial layers, which results in an increased absorption in the ultraviolet region below 280 nm and luminescence quenching may occur as well. Molar ratios of oxides are in Table 5.1.

	PbO	B_2O_3	Al_2O_3	Y_2O_3	CeO_2
[mol]	0.898297	0.078569	0.021076	0.005571	0.001906

Table 5.1: Molar ratios in the PbO-based melt for the 5C series. The total amount of oxides was 100-200 g.

$BaO - BaF_2 - B_2O_3$ flux

The BaO-based flux is nonvolatile, nontoxic, with negligible chemical reactivity with the platinum crucible. Barium atoms are much bigger compared with lead atoms. Therefore they cannot be incorporated into garnet lattice since there is not enough space for them. The disadvantages are higher viscosity and high surface tension of the solvent which leads to etching of the epitaxial layer after withdrawing the substrate from the melt. Mechanical and chemical cleaning of the film is necessary due to strong adhesion of the solvent. On the other hand, the BaO-based flux provides epitaxial films of better purity, higher light yield, and much lower UV absorption, however with worse crystal and surface quality. Molar ratios of oxides are in Table 5.2.

	$BaCO_3$	B_2O_3	Al_2O_3	Y_2O_3	BaF_2	CeO_2
[mol]	0.273653	0.203217	0.106191	0.064358	0.205327	0.003747

Table 5.2: Molar ratios in the BaO-based melt for the 5YBC series. The total amount of oxides was 100-200 g.

5.4 Epitaxial films

Ce doped epitaxial garnet films ($Ce_xY_{3-x}Al_5O_{12}$) were prepared by the LPE method on pure YAG and LuAG substrates, see Fig. 5.3. The scheme of the sample is shown in Fig. 5.2. On both surfaces of the substrate there are thin films doped by Ce. The YAG crystal for substrates, grown by the Czochralski method, was received from the Crytur company in

Turnov. It has a crystallographic orientation of (111), a diameter of 20 mm and was cut to 0.5 mm thick slices and chemically polished, Fryštacký. The quality of some epitaxial layers was confirmed by X-ray structural analysis. The results are summarized in Table 5.3.

Sample	Thickness	Lattice constant
1C4	substrate	12.0093(1)Å
1C3	10.69 μm	12.0114(1)Å
3C2	2.86 μm	12.0107(1)Å

Table 5.3: Results from X-ray structural analysis of YAG substrate (1C4), and Ce:YAG epitaxial layers (1C3, 3C2) on YAG substrate, oriented (111). The lattice constants were determined from the positions of diffractive maxima.

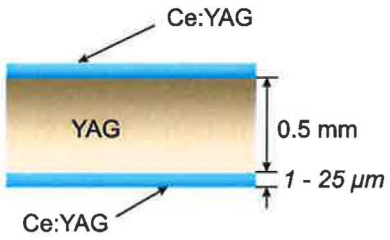

Figure 5.2: Schematic diagram of the sample. Thin films of Ce:YAG are on both sides of the YAG substrate.

Film thickness

As the refractive index difference between the film and the substrate is small, the common interferometric technique cannot be used. Film thickness was determined by weighting the substrate before and after the LPE on a precise analytical balance Mettler Toledo. The thickness d of the layer can be calculated as:

$$d = \frac{1}{2\pi r}\frac{m}{\rho}, \tag{5.2}$$

m is difference in weight and ρ is the density of the material, Table 4.1. After doping by cerium the change in density is negligible. As shown in Fig. 5.3A the substrate has a round shape with a radius of r=1 cm.

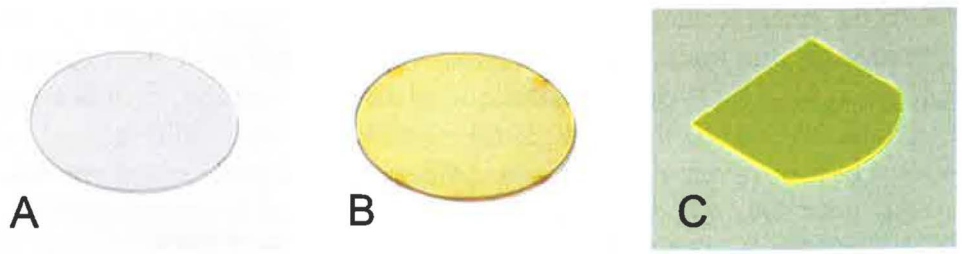

Figure 5.3: Photos of samples: **A** YAG substrate, **B** Ce:YAG thin film on the YAG substrate prepared by LPE, **C** Ce:YAG single crystal prepared by the Czochralski method, provided by J. Kvapil, Monokrystaly Turnov.

Chapter 6

Experimental technique

In this work, optical methods were used for the examination of optical properties of Ce:YAG, Ce:LuAG epitaxial layers prepared by the LPE method in the spectral range from 200 nm to 1000 nm, at room temperature. Ce:YAG, Ce:LuAG samples were characterized by: X-ray structural analysis, Table 5.3, electron probe microanalysis (EPMA), Chapter 7, light yield measurements at α-particles, [27], absorption, excitation, emission, and kinetic measurements.

Absorption spectra provide basic information about the material. They show the fraction of incident electromagnetic radiation absorbed by the material over certain spectral range and can be used to identify impurities present in material. The luminescent spectra are a detailed source of information about optical transitions in the material. The excitation spectrum illustrates luminescence produced over a range of wavelengths of incident light. The emission spectrum can be used to determine impurities in the material. The measured intensity of luminescence represents relative intensity. In our experimental arrangement, it is not possible to measure the absolute intensity. We can compare the shape of luminescent spectra rather than their intensity. The intensity depends strongly on sample position in the holder and on the angle of incidence of the excitation beam, discussed below Section 6.3. The same conditions could not be kept, because samples have different surface quality, and were cut in different shapes, 7×7 mm squares or semilunar. Decay curves provide information about luminescence kinetics, transitions in the material and decay time of luminescence.

6.1 Absorption spectra

Transmission spectra were measured using a double beam spectrometer Perkin Elmer, Lambda 12. It consists of a light source (VIS and UV lamp), a monochromator, which is used to select a single wavelength from the emission spectrum of the lamp and to scan over a desired spectral range, a sample holder, followed by a photodetector. The light of the lamp is separated into two beams. The reference beam is coming through the pure sample of YAG single crystal without any layers. The second beam passes through the measured sample as shown in Fig. 6.1. In this setting it is not necessary to carry out the reflection correction, since the refractive indices of YAG and Ce:YAG are almost identical. From transmission we can calculate the absorption coefficient α using:

$$\alpha = -\frac{1}{2d} ln(\frac{T}{100}), \tag{6.1}$$

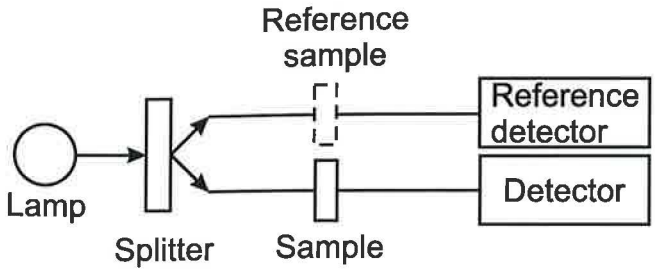

Figure 6.1: Scheme of the double-beam spectrophotometer used for the measurement of absorption. The illuminating beam is split into two beams, which are directed towards two different channels: a reference channel and a sample channel. The output intensities are detected by two similar detectors.

where d is the thickness of one layer and T is the transmission percentage. Transmission was recorded in the spectral range from 200 nm to 1000 nm with a spectral resolution of 1 nm.

Transmission of pure YAG and LuAG substrates was recorded in a different experimental setup without a reference sample in the reference beam. In this case, the reflection correction had to be carried out according to the equation:

$$T = \left(1 - R^2\right) \frac{e^{-\alpha d}}{1 - R^2 e^{-2\alpha d}}, \tag{6.2}$$

where d is the thickness of the crystal, α is the absorption coefficient and R is reflection coefficient, which depends on the refractive index n at normal incidence:

$$R = \frac{(n-1)^2}{(n+1)^2}. \tag{6.3}$$

The refractive index of YAG and LuAG changes with the wavelength of incident light, see Figs. 6.2, 6.3. Experimental data was fitted in the Origin program.

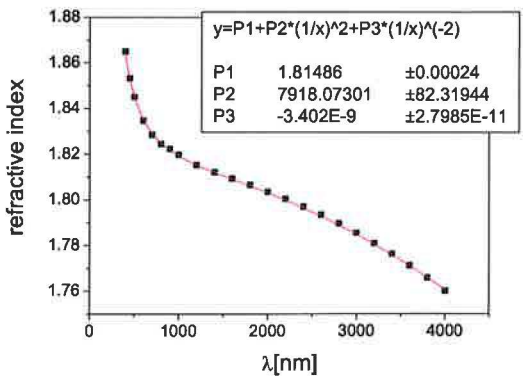

Figure 6.2: Refractive index of YAG as function of wavelength, Bond [28].

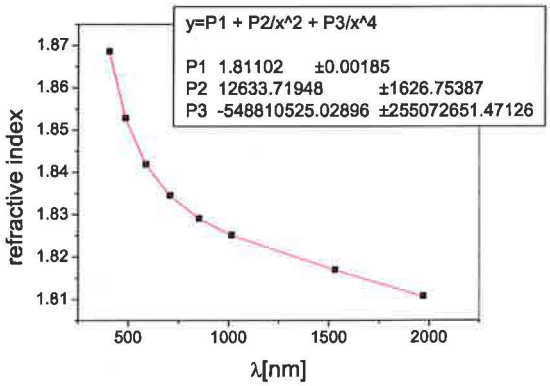

Figure 6.3: Refractive index of LuAG as function of wavelength, Kuwano et al. [16].

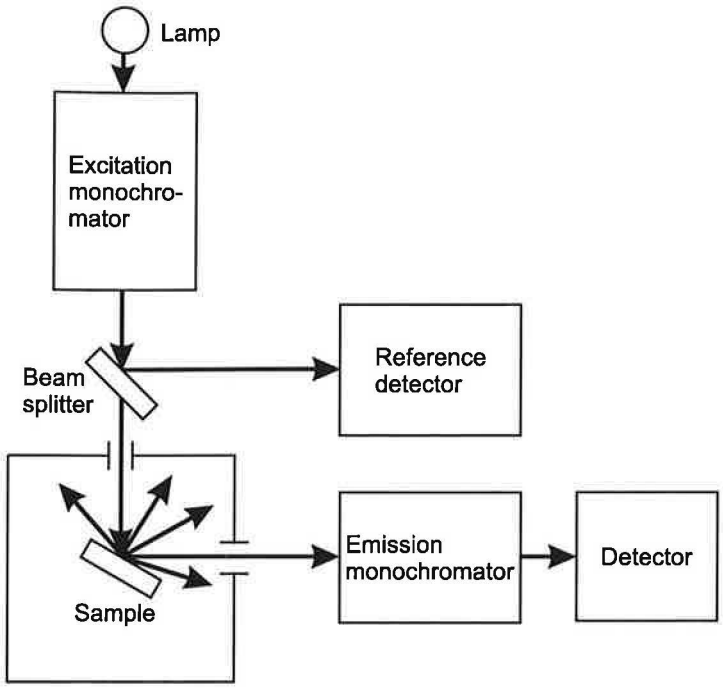

Figure 6.4: Schematic diagram of the luminescence spectrometer.

6.2 Luminescent spectra

Luminescent spectra were measured by spectrometer Fluoro Max-3, JY Jobin Yvon Horiba. The excitation wavelength is selected from the spectrum of the excitation lamp by the monochromator. The light emitted by the sample is registered by the photodetector. A part of the light of the excitation source is detected by the reference detector. Luminescent radiation is emitted in all directions. Various experimental geometries are used to collect luminescence. In our case the angle of incidence is 30°, Fig. 6.5, to prevent the excitation light reflected from the surface of the sample from reaching the detector, see Fig. 6.4. Two kinds of spectra, emission spectra and excitation spectra, can be registered.

Excitation spectra

The excitation spectrum is the dependence of intensity of luminescence at a fixed selected wavelength on the wavelength of the excitation light. The intensity of radiation of the lamp changes with wavelength. The excitation spectra were standardized by dividing by the reference spectrum of the excitation source. A 500 nm edge filter was placed in front of the slit of the emission monochromator to prevent the excitation light from reaching the detector. The samples were excited at wavelengths in the spectral range of 220-520 nm with a spectral resolution of 0.5 nm. The emission was collected at the wavelength of 550 nm. For low absorbing samples, as is our case, the excitation spectrum copies the shape of the absorption spectra as shown in Chapter 7.

Emission spectra

The sample is excited at a fixed wavelength. The emission spectrum is the dependence of the luminescence intensity on the wavelength of luminescence. The emission spectra were measured on Ce doped YAG and LuAG by exciting at two different wavelengths utilizing

various edge filters in emission and excitation beams, see Table 6.1. Emission spectra were not corrected to spectral distribution of the excitation light, sensitivity of the photodetector, or transmissivity of the monochromators.

	Excitation wavelength [nm]	Emission wavelength [nm]	Filter in excitation beam	Filter in emission beam
Ce:YAG	455	470-750	blue	450
	340	360-750	UG2	400
Ce:LuAG	445	470-750	blue	450
	345	360-750	UG2	400

Table 6.1: Measurement parameters of the emission spectra. The blue filter has its transmission maximum at 445 nm. The UG2 filter has its transmission maximum at 360 nm and 380 nm it transmits 48% of incoming light.

6.3 Dependence of the intensity of luminescence on the experimental geometry

The intensity of luminescence depends strongly on the sample position in the holder and on the angle of incidence, Fig. 6.5. The sample is fixed in the holder by four clamps. Its position can be changed and it is possible to measure luminescence intensity in different places on the surface of the sample. This was examined on the semilunar crystal, Fig. 6.7. When the trace of the excitation beam on the surface of the crystal was close to its straight edge, the light output rose steeply. This points to some light guiding effect and to multiple reflection on the crystal edge. The light output also varies with the angle of incidence. The emission spectra were measured for establishing this effect at 455 nm for various angles on the sample Fig. 6.7. Fig. 6.6 illustrates the change in the intensity of the emission maximum for two different positions of the sample. In position 1, the trace of the excitation beam was nearly at the edge of the crystal. However, position 2 was in the middle of the sample. The luminescent measurements, see Chapter 7, were made at the angle of incidence of 30°.

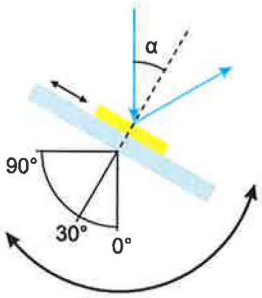

Figure 6.5: Sketch of the sample holder for the luminescent measurement. The holder can be turned around its vertical axis. The position of the sample fixed in the holder can be changed. α is the angle of incidence of the excitation beam.

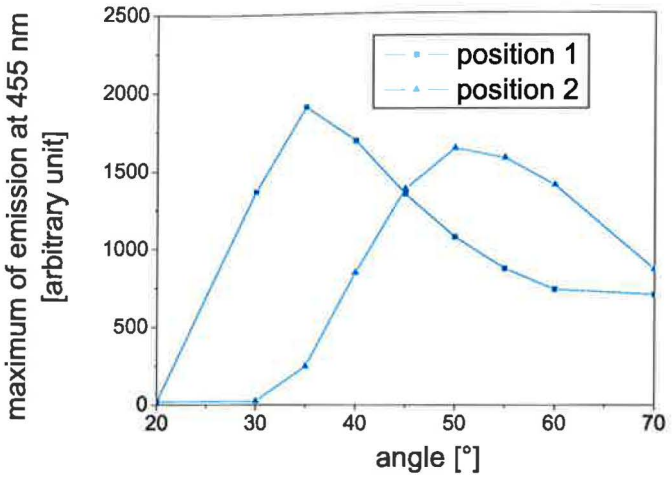

Figure 6.6: Dependence of the emission maximum on the angle α for the sample of semilunar shape. The luminescence intensity was measured in two positions: position 1 was nearly at the edge of the crystal, position 2 was in the middle of the sample.

Figure 6.7: Photograph of Ce:YAG thin film on the YAG substrate prepared from the BaO flux cut into semilunar shape.

6.4 Kinetics of luminescence

Decay curves of luminescence were measured by the single photon counting method. This method is based on the measurement of the time interval between the pulse excitation of the sample and the detection of the first luminescence photon in the detection photomultiplier. As a result, we obtain a distribution of probability of number of photons depending on the time interval. Optical and electronic equipment will be discussed separately.

Optical part of equipment

A hydrogen lamp was used as an excitation source with a pulsewidth of 1 ns and repetition rate 20 kHz. The pulse shape of the hydrogen lamp does not depend on wavelength. The light from the lamp is coming through the excitation monochromator and hits the sample at an angle of 45°, Fig. 6.8. Luminescence radiation emitted by the sample passes the emission monochromator and is reaches the photomultiplier, where the first incoming photon is being registered. An edge filter is inserted in front of the emission monochromator, in this case 500 nm edge filter, to prevent the excitation wavelength from reaching the detector.

Electronic part of equipment

Scheme of the electronic equipment is shown in Fig. 6.9. A flash of the lamp performs a starting pulse for the initialization of the time interval measurement. The light is guided into a synchronizing photomultiplier; it is formed in a shaping unit and is led away into a time-to-amplitude converter (TAC). The TAC is the heart of the equipment. The pulse created by the impact of the first photon of luminescence is modified in the shaping unit and guided

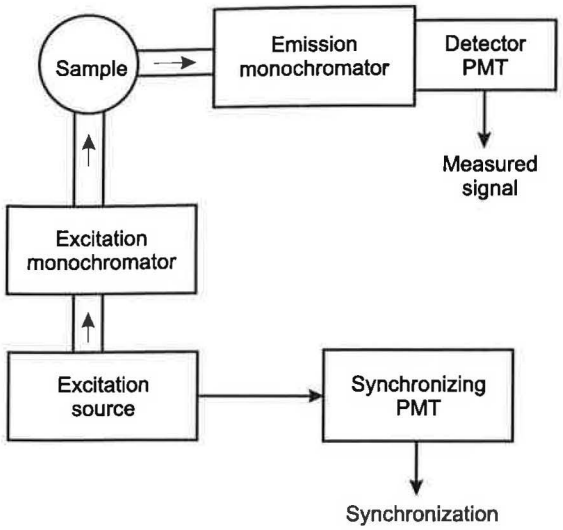

Figure 6.8: Scheme of optical part of equipment.

into the TAC as a stopping pulse and it ends the time measurement. The TAC converts the time interval between the excitation pulse and the registration of the first photon to a certain value of voltage. Multichannel analyzer assigns incoming voltage to the corresponding channel according to its size. This process is repeated many times. As a result the decay curve of luminescence is drawn on the computer screen as the dependence of the number of photons on time. The measured signal has to fulfill the condition, that the number of photons impacting the photomultiplier in 1 s cannot exceed 2-3 % of the counting rate of the source. Otherwise the characteristic can be distorted towards shorter times. In the delay unit, the delay was set to 160 ns to establish the intensity of background radiation.

The luminescence was measured at room temperature. The samples were excited at λ=340 nm. The emission was collected at λ=530 nm. The samples were measured over a period of one to two hours according to their luminescence intensity.

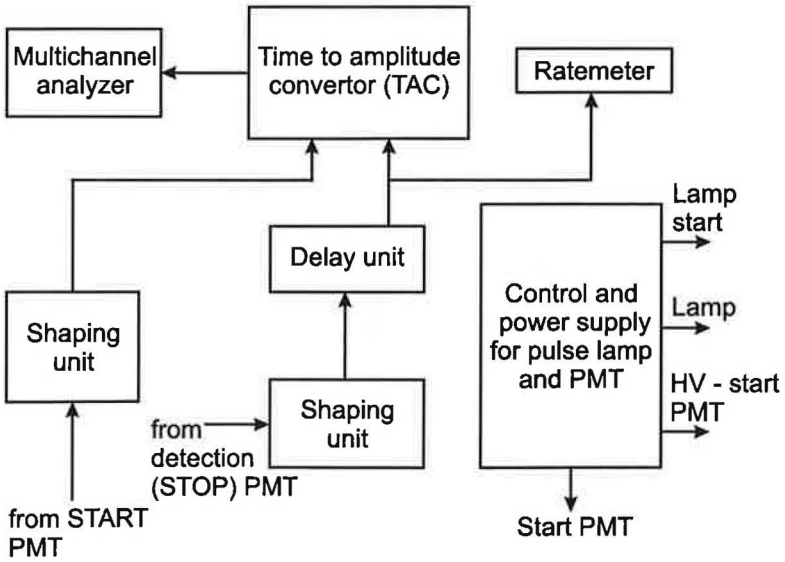

Figure 6.9: Scheme of electronic evaluation part of equipment.

Chapter 7

Results and discussion

The optical spectra of the samples prepared under different conditions by the LPE method are discussed in this chapter. The samples were grown from the melts of different composition and at different growth temperatures, Tables 7.2, 7.3. They vary in the concentration of cerium and impurities, in the layer thickness, in the surface quality and they were cut in different shapes (7×7 mm squares and semilunar). We look for ideal growth conditions. We are interested in how the concentration of cerium and impurities is affected by melt composition and how the optical spectra are influenced.

7.1 Ce:YAG

7.1.1 Optical properties of the samples prepared from the PbO-B_2O_3 flux

The Ce:YAG epitaxial films on YAG substrates were prepared by the LPE, see Chapter 5. The absorption, the excitation and the emission spectra were measured using commercial spectrometers, Chapter 6. These spectra are displayed in Figs. 7.3 - 7.22. The kinetics of luminescence was measured in cooperation with the Institute of Physics of the Academy of Sciences, see Section 6.4. The samples prepared from the PbO-based flux have high quality surface only with a small amount of defects, see Fig. 7.1.

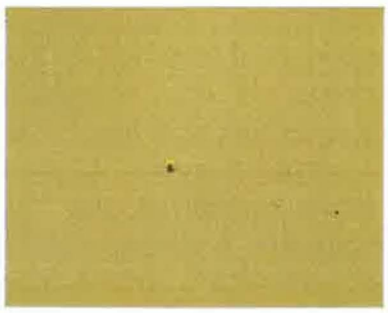

Figure 7.1: Photograph of surface of the sample 5C4 prepared from the PbO-based flux. The surface is very homogenous. There are only a few defects.

The concentration of cerium in the epitaxial films can be established from the comparison of absorption coefficients with Ce:YAG single crystal. The absorption is proportional

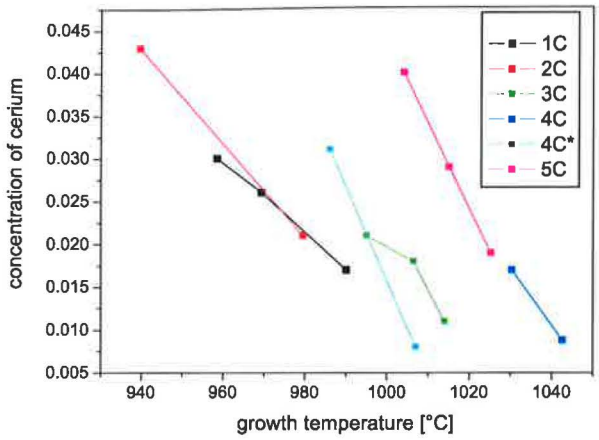

Figure 7.2: Concentration of cerium in $Ce_xY_{3-x}Al_5O_{12}$ thin films as a function of growth temperature. Series 1C - 5C were grown from various solutions.

to the number of absorbing centres. High-quality Ce:YAG single crystal, from Monokrystaly Turnov, has 0.5 weight percent of cerium. This amount corresponds to $x = 0.02$ in $Ce_xY_{3-x}Al_5O_{12}$. The maxima of the peak at 458 nm (2.7 eV) were compared with the maximum of Ce:YAG single crystal and the cerium concentration in the layers was calculated. The results are displayed in Table 7.2. The sample compositions were also analysed by the electron probe microanalysis (EPMA). This method do not provides enough accurate values, because the contentrations are below the detection limit of this method ($x \leq 0.01$). Cerium concentrations determined from the absorption coefficient give us more reasonable values.

Concentration of cerium is a function of growth temperature, Fig. 7.2. For higher growth temperatures, a smaller amount of cerium ions is incorporated in the layer. At lower growth temperatures higher concentration of both cerium ions and also impurities is incorporated into the layer. This affects the luminescence intensity, because it is a function of concentration of activator ions (cerium).

Absorption spectra

The absorption spectra of the Ce:YAG epitaxial films prepared from the PbO-based flux are displayed in Figs. 7.3, 7.7, 7.11, 7.15, and 7.19. The absorption coefficient α was calculated from transmission using Equation 6.1 and it is plotted in dependence on energy in eV. The two broad peaks observed at 458 nm (2.7 eV) and 340 nm (3.6 eV) correspond to transitions from the ground state $4f$ of Ce^{3+} into its excited states $5d$. According to energy level diagram, see Fig. 4.4, five peaks are expected in absorptions spectra of Ce:YAG, see ideal spectrum of Ce:YAG single crystal in Fig. 7.47. The high energy transition at 230 nm (5.4 eV) is not distinguishable here, because it overlaps with the increasing absorption above 5 eV (248 nm). This absorption originates from impurities in layers (Pb-from flux, Pt-from platinum crucible).

Luminescent spectra

The measurement of the luminescence intensity is relative. The light output of various samples could not be compared easily. It is strongly affected by the position of the sample in the holder, by the angle of incidence, Section 6.3, and also by the quality of the surface of the crystal and the shape of the sample. Nonuniformities and scratches can scatter the light and therefore influence the light output.

The excitation spectra are plotted in dependence on wavelength in nm, Figs. 7.4, 7.8, 7.12, 7.16, and 7.20. They have a similar shape as the absorption spectra. Two peaks are observed at 455 nm and 340 nm corresponding to transitions between levels of the Ce^{3+} ion, Fig. 4.4. The peak expected at 230 nm is overlapped in all samples grown from the PbO-based flux. The emission spectra show a broad band centred at 530 nm and composed of two contributions, Tomiki [19]. This is connected with two manifolds $^2F_{5/2}$, $^2F_{7/2}$, in which the ground state of the Ce^{3+} ion is split. The emission spectra were excited at λ=455 nm, see Figs. 7.5, 7.9, 7.13, 7.17, and 7.21, and at λ=340 nm, see Figs. 7.6, 7.10, 7.14, 7.18, and 7.22.

Series 1C - 4C

The concentration of garnet constituents $Y_2O_3 + Al_2O_3$ in the melt was increased from 1C to 4C series of the samples. The sample 4C5 was prepared from the melt, to which 0.03 g of CeO_2 was added compared to the previous series, see 4C* series in Fig. 7.2.

The order of samples in absorption spectra corresponds to their growth temperature. The lower growth temperature, the higher absorption coefficient at 2.7 eV. This is due to higher concentration of cerium and impurities incorporated in layers at lower temperatures, as is discussed above. The absorption spectra differ from the ideal spectrum of Ce:YAG single crystal, Fig. 7.47. They shows increased absorption in the region between 3 eV and 3.5 eV and the absorption coefficient is rising steeply above 5 eV. Both features originate probably in impurities. Pb absorbs around 4.75 eV (260 nm), Babin et al. [29].

The highest light output was achieved in the samples with the highest thickness and concentration of cerium. The sample 2C3 has a higher amount of cerium and a higher thickness compared to the sample 2C2, but lower luminescence intensity, Figs. 7.8-7.10. It was prepared at lower temperature, Table 7.2. Hence, it contains higher concentration of Pb, Pt impurities. In the excitation spectra the increasing intensity below 250 nm is observed. It is probably unreal, because the samples are strongly absorbing in this spectral range. Some feature extending between 400 nm and 450 nm appears in emission spectra excited at 340 nm, Figs. 7.6, 7.10, 7.14, 7.18. First, it was observed in the spectrum of the sample 1C5. It is missing in the spectra of samples 1C2 and 1C3, Fig. 7.6. The sample 1C5 was prepared one day later. The origin of this feature is not clear. It may be connected with some unknown impurity.

Series 5C

PbO used for the preparation of the 1C - 4C series contained high concentration of Fe impurity, see Table 7.1. Fe can strongly quench the luminescence even in small concentration, see Section 7.3. Therefore, 5C series was prepared from new PbO of much higher purity.

The absorption spectrum of the sample 5C2, the first prepared sample from this series, shows a very nice shape Fig. 7.19. It shows almost zero absorption between 3 eV and 3.5 eV,

compared to the other samples grown from the PbO-based flux, discussed above. Moreover its absorption spectrum is very similar to that of Ce:YAG single crystal in this spectral range, Fig. 7.47. Unfortunately, the two following samples 5C3, 5C4 have increasing absorption in this region again. Probably, the melt was contaminated. The steeply rising absorption above 5 eV originating in impurities seems to be a typical feature of the absorption spectra of the samples prepared from the PbO-based flux.

The whole 5C series shows much higher light output compared to the 1C - 4C series, at least of one order of magnitude, Figs. 7.20-7.22. The sample 5C2 has the greatest thickness, see Table 7.2 and therefore the highest light output. The lowest luminescence intensity was measured for the sample 5C4. It was prepared at lower temperature, Table 7.2. Hence, it contains cerium in high concentration but also Pb and Pt impurities, Fig. 7.19. The feature observed in 1C - 4C series, see above, in the spectral range from 400 nm to 450 nm is missing in the emission spectra of 5C series, Fig. 7.22, since the new PbO, from which 5C series was grown, is much purer than the one applied previously (series 1C - 4C) and contains only a small amount of impurities.

	PbO [mg/kg]	Ce:YAG [mg/kg]
Fe	107	259
V	<1	<1
Cr	<5	<5
Mn	<1	<1
Ni	<2	<2
Co	<2	<2
Mo	<10	<10

Table 7.1: Amount of impurities present in the PbO and Ce:YAG melt used for the preparation of the sample 4C4.

Kinetics of luminescence

The kinetics of luminescence represents a very sensitive method to determine impurities or defects in materials compared to absorption and emission spectra and provides new valuable information. Decay curves were measured by the single photon counting method, Section 6.4. The samples were excited at λ=340 nm and the luminescence was collected at λ=530 nm at room temperature. The absorption and luminescence spectra of 1C - 5C series, discussed above, show that some impurities are incorporated in thin films. In decay characteristics some nonlinearity is present, see Figs. 7.23-7.26. Hence, it is not one-exponential decay. In the Spectra Solve program, deconvolution was performed and decay curves were fitted by Equation 2.6. All spectra of thin films prepared from the PbO-based flux show two-exponential decay, Figs. 7.23-7.26. It can be explained that some impurities are present in the layers and partly quench the luminescence. From the fitted functions of 1C series it follows that there are two fast components with comparable amplitudes. The fitted function for the sample 5C2 is:

$$I(t) = 7559 * exp(-t/58.2ns) + 1938 * exp(-t/20.5ns) + 4.8. \quad (7.1)$$

It exhibits mild non-exponential behaviour and shortening of the decay time (58.2 ns) compared to Ce:YAG single crystal (about 62 ns at room temperature, Table 4.1). In other words, some energy transfer may occur and the luminescence is partly quenched. The amount of energy of the excited state lost due to nonradiative transition into some trap can be expressed quantitatively using the following method. The fit of the sample 5C2, Equation 7.1, was normalized to 1 in t=0 and integrated. Afterwards, normalized theoretical decay $1 * exp[-t/62ns]$ was integrated, too. The ratio of these two integrals gives us the value 0.95. This indicates that 5% of energy was lost in the sample 5C2. It contains almost zero concentration of Fe, but Pb, Pt impurities are still included. The quantum efficiency of luminescence of the samples 1C2, 1C3, 1C5 was reduced due to nonradiative transition by 22%, 53%, 53%, respectively.

From our measurements follows that some impurities are contained in samples prepared from the PbO-based flux. They cause the nonradiative transitions. As a result two-exponential decay and decrease of light yield in emission spectra are observed. We eliminated Fe impurity, sample 5C2, but some component, which may be connected with Pb, is still present. Therefore, we decided to search for the flux without Pb.

Sample	Thickness [μm]	Growth temperature T_g [°C]	Ce concentration x=
Ce:YAG thin films prepared from the PbO-based flux			
1C2	11.87	990	0.017
1C3	10.69	969.3	0.026
1C5	8.83	958.5	0.030
2C2	5.41	979.5	0.021
2C3	8.74	939.5	0.043
3C1	14.56	1006.4	0.018
3C2	2.86	995	0.021
3C3	7.33	1014	0.011
4C1	21.13	1030.3	0.017
4C2	7.96	1042.6	0.009
4C4	25.42	986	0.031
4C5	10.18	1007	0.008
5C2	12.77	1015	0.029
5C3	12.21	1025.2	0.019
5C4	8.03	1004	0.040
Ce:YAG thin films prepared from the BaO-based flux			
4YBC1	0.99	942	0.037
5YBC1	4.40	939.1	0.070
5YBC2	6.97	942.7	0.059
5YBC3	5.63	933.6	0.067
Ce:LuAG thin films prepared from the BaO-based flux			
1LC1	1.74	936	0.168
1LC2	1.91	928.8	0.113

Table 7.2: Thickness, growth temperature and Ce concentration for Ce:YAG and Ce:LuAG epitaxial layers prepared from the PbO-based and the BaO-based fluxes.

Sample	Thickness [μm]	Growth temperature T_g [°C]
YAG thin films prepared from the PbO-based flux		
1YAG1	13.96	989
1YAG2	6.03	1003.5
2YAG1	24.27	1011.5
2YAG2	2.41	1030.2
5C1	23.65	1015.4
YAG thin films prepared from the BaO-based flux		
3YB2	5.30	938
3YB3	1.23	920
3YB4	1.64	946
5YB1	5.19	939.4
LuAG thin films prepared from the BaO-based flux		
1L1	1.85	945
1L2	2.50	936.5

Table 7.3: Thickness and growth temperature for YAG and LuAG epitaxial layers prepared from the PbO-based and the BaO-based fluxes.

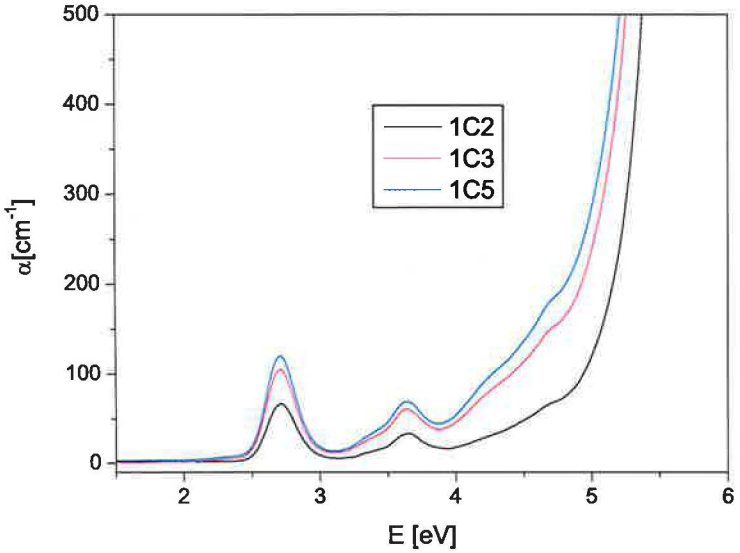

Figure 7.3: Absorption spectra.

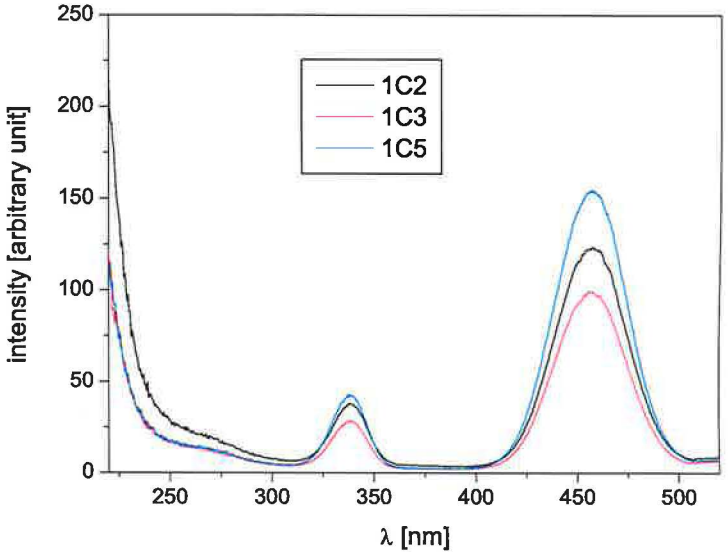

Figure 7.4: Excitation spectra at λ_{em}=550 nm.

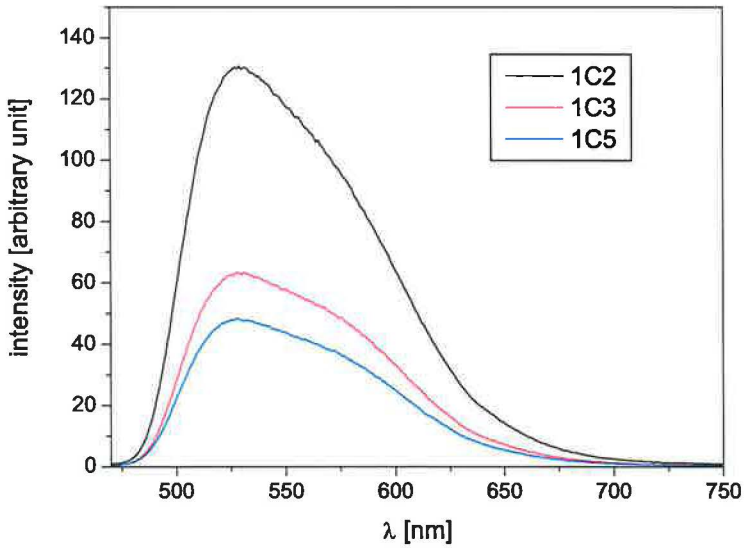

Figure 7.5: Emission spectra at λ_{ex}=455 nm.

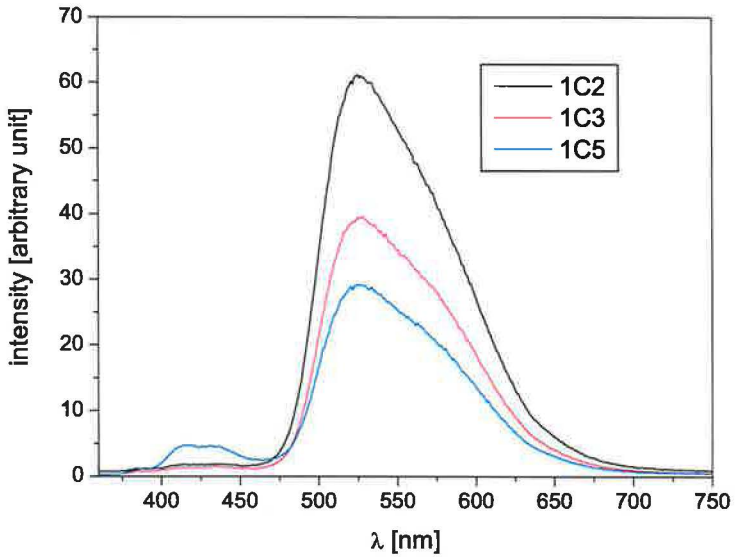

Figure 7.6: Emission spectra at λ_{ex}=340 nm.

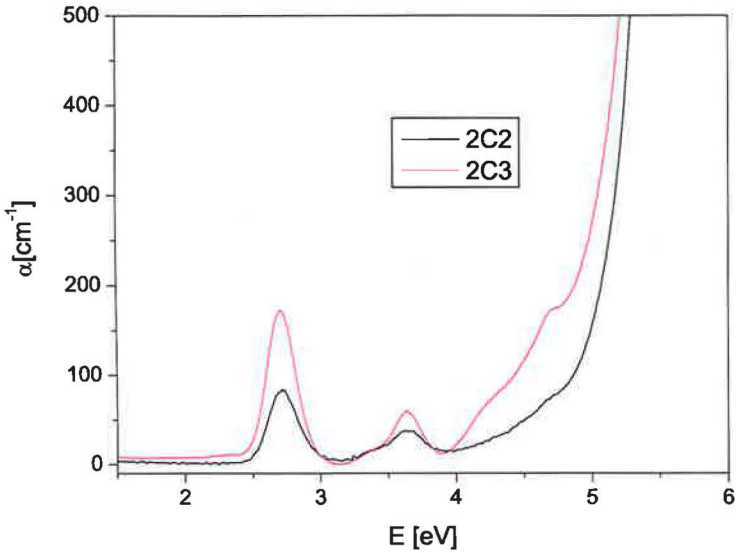

Figure 7.7: Absorption spectra.

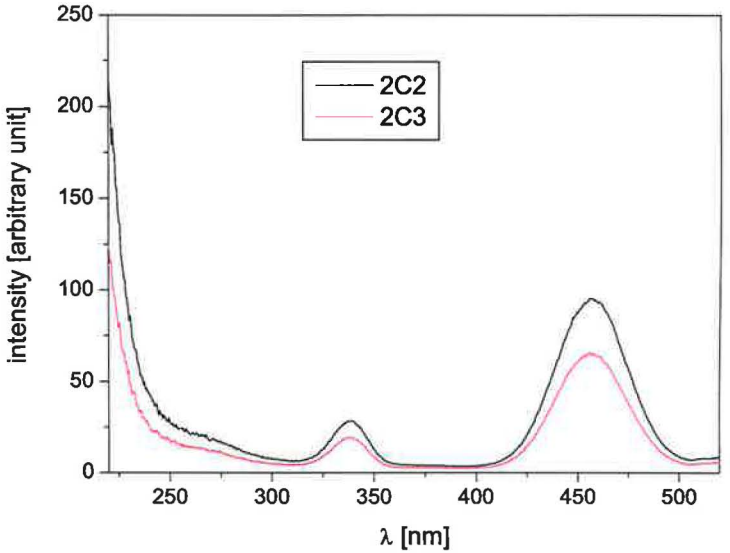

Figure 7.8: Excitation spectra at λ_{em}=550 nm.

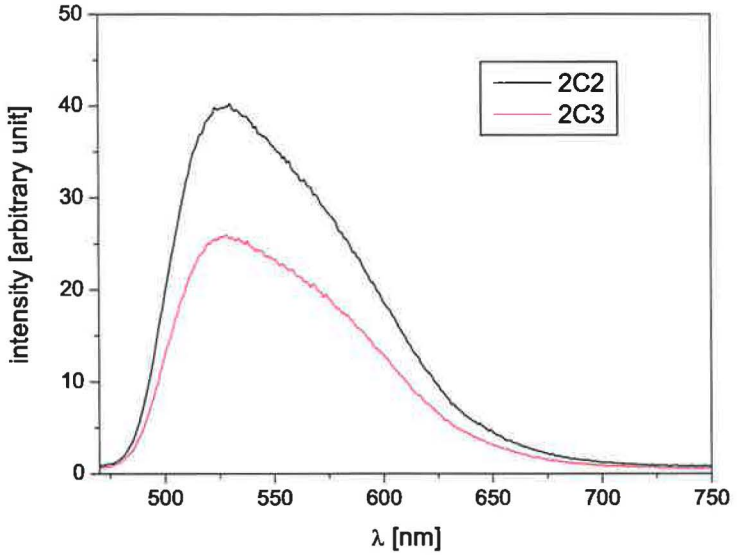

Figure 7.9: Emission spectra at λ_{ex}=455 nm.

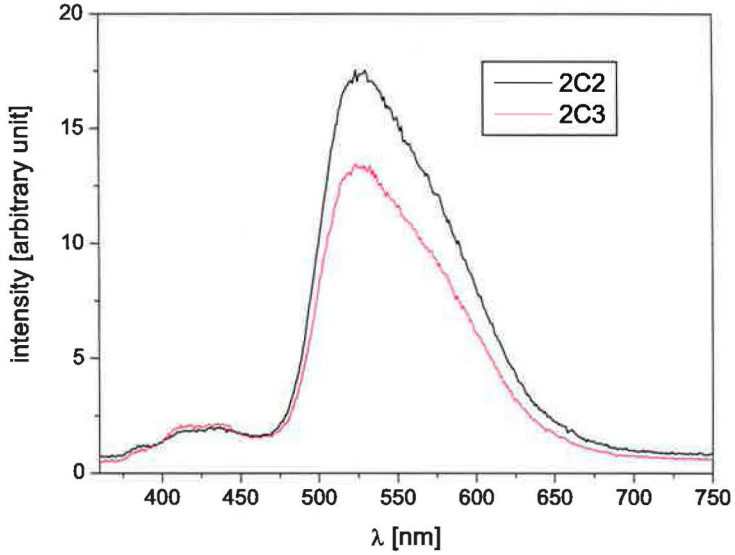

Figure 7.10: Emission spectra at λ_{ex}=340 nm.

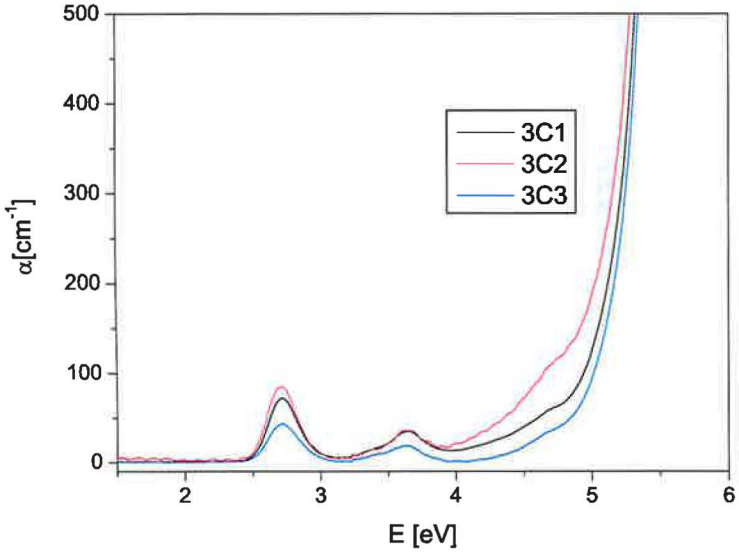

Figure 7.11: Absorption spectra.

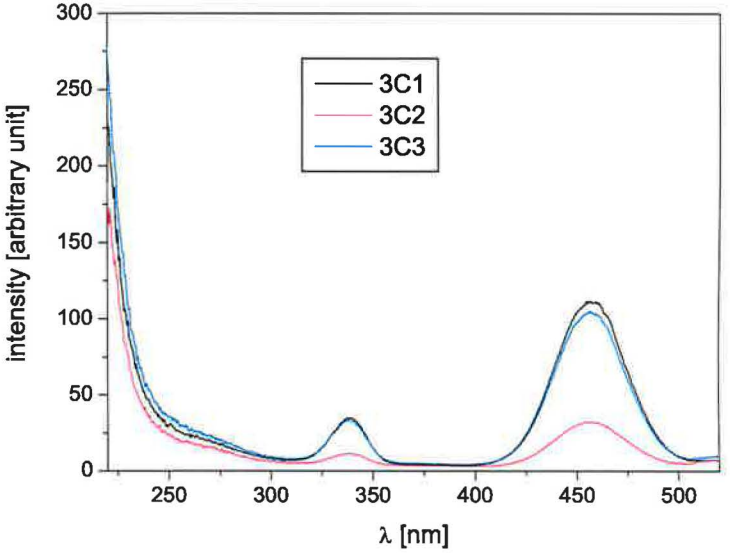

Figure 7.12: Excitation spectra at λ_{em}=550 nm.

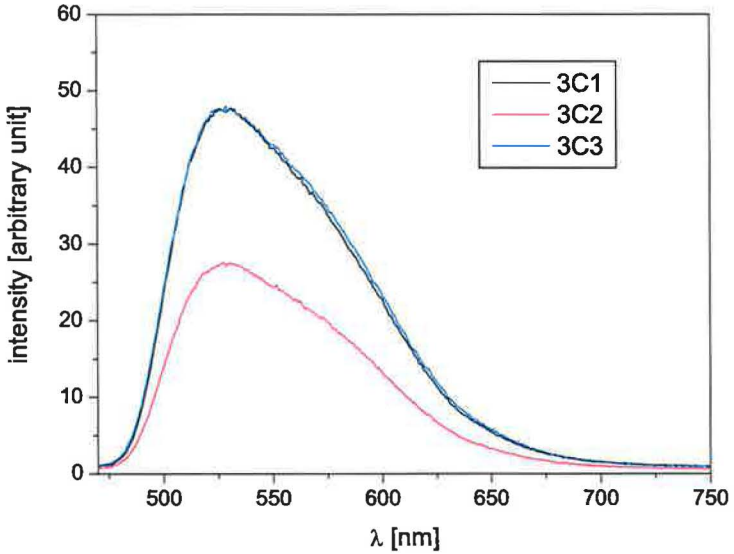

Figure 7.13: Emission spectra at λ_{ex}=455 nm.

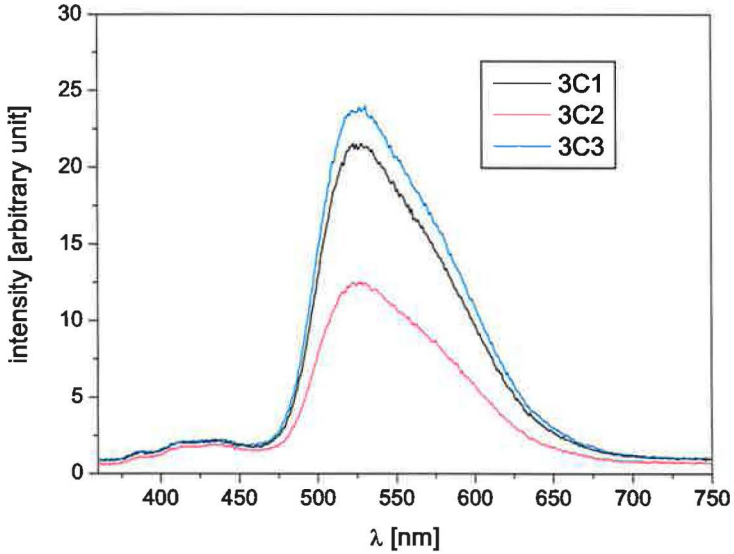

Figure 7.14: Emission spectra at λ_{ex}=340 nm.

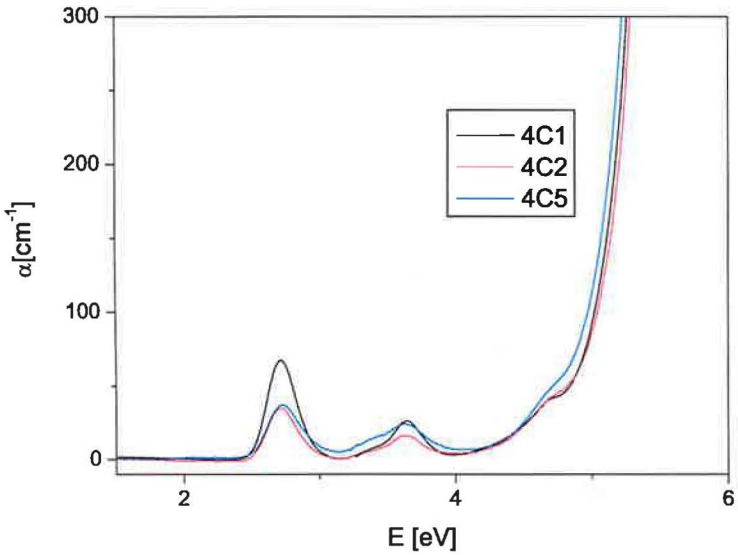

Figure 7.15: Absorption spectra.

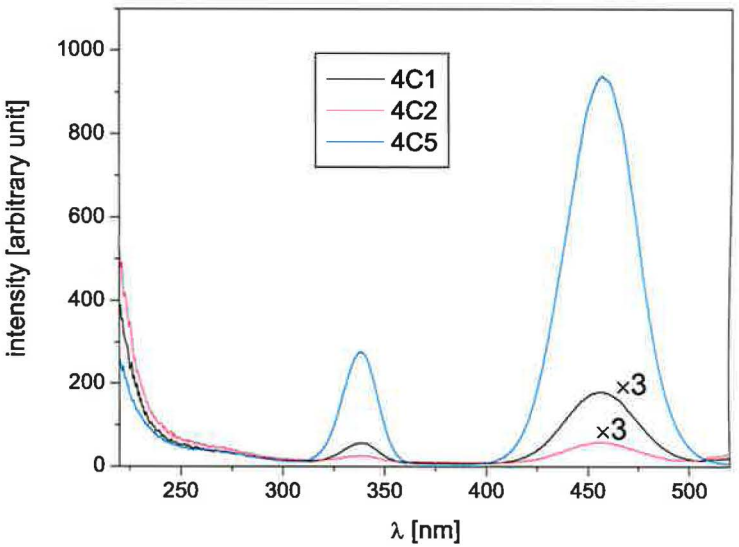

Figure 7.16: Excitation spectra at λ_{ex}=550 nm.

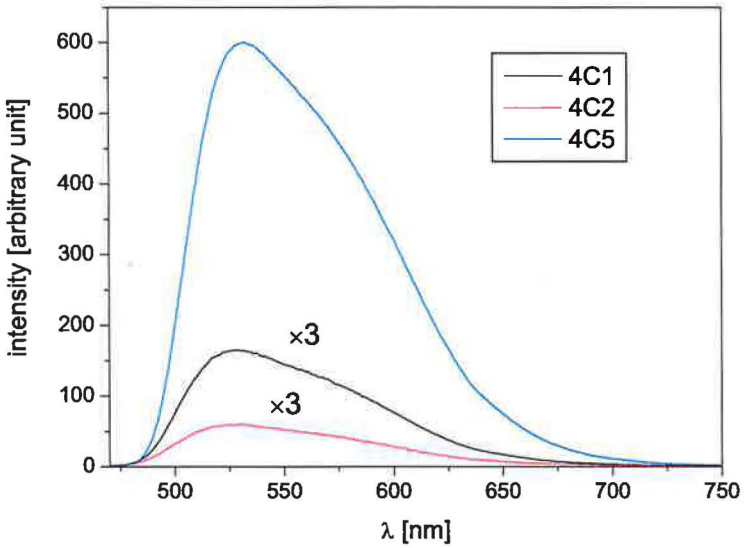

Figure 7.17: Emission spectra at λ_{ex}=455 nm.

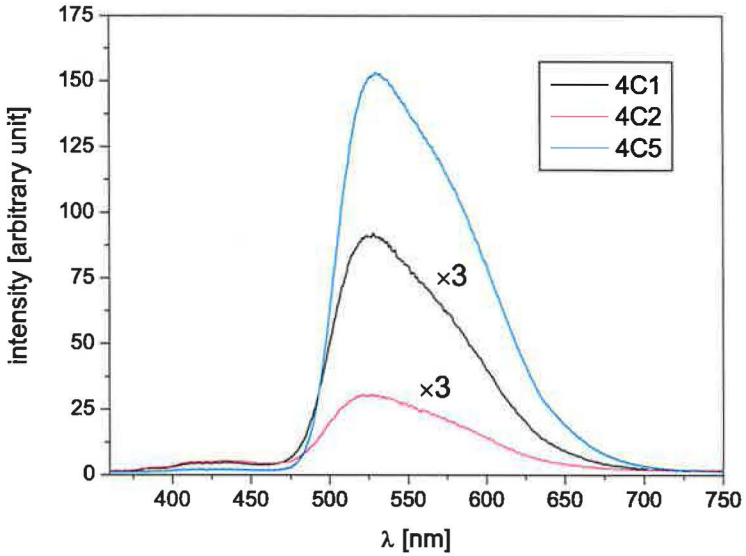

Figure 7.18: Emission spectra at λ_{ex}=340 nm.

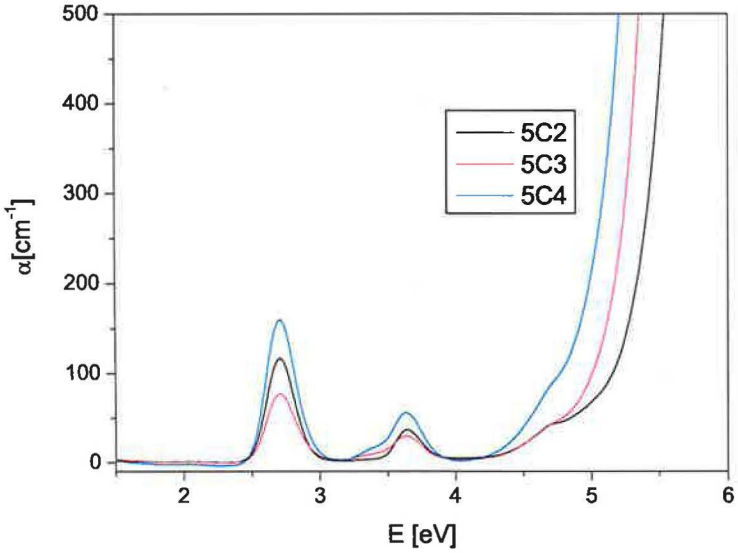

Figure 7.19: Absorption spectra.

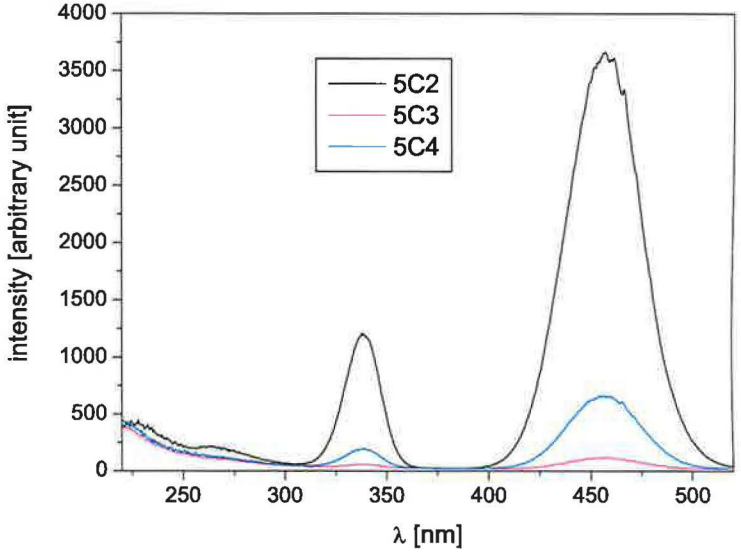

Figure 7.20: Excitation spectra at λ_{em}=550 nm.

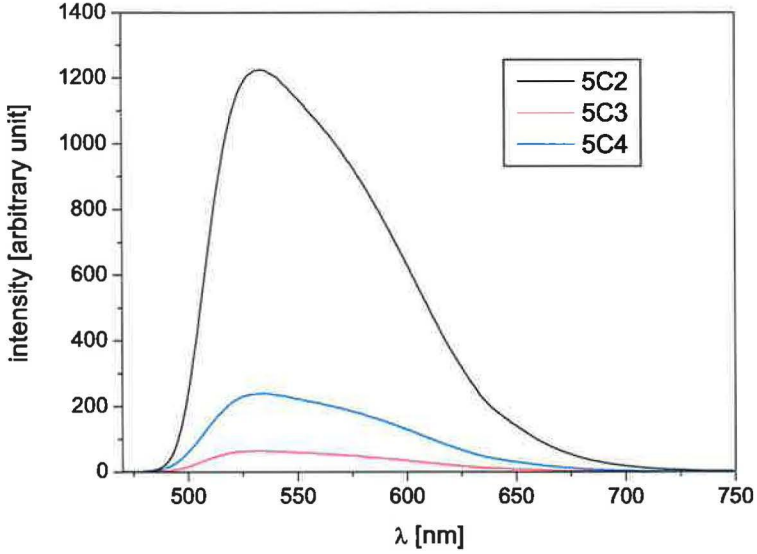

Figure 7.21: Emission spectra at λ_{ex}=455 nm.

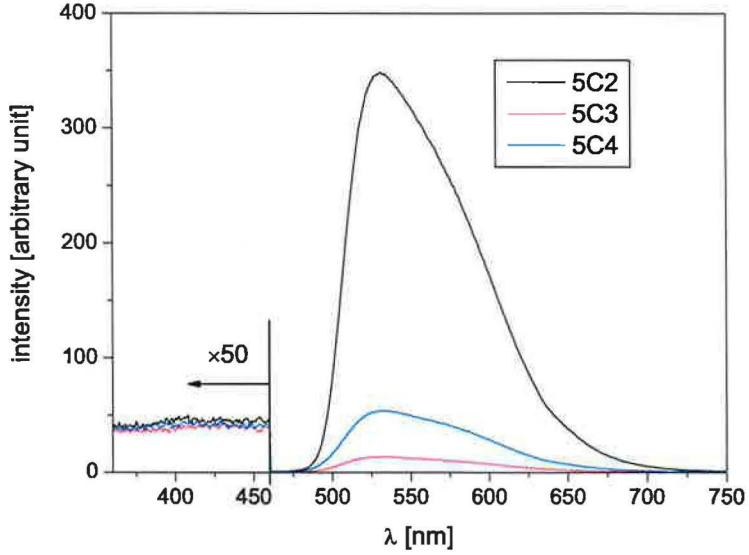

Figure 7.22: Emission spectra at λ_{ex}=340 nm.

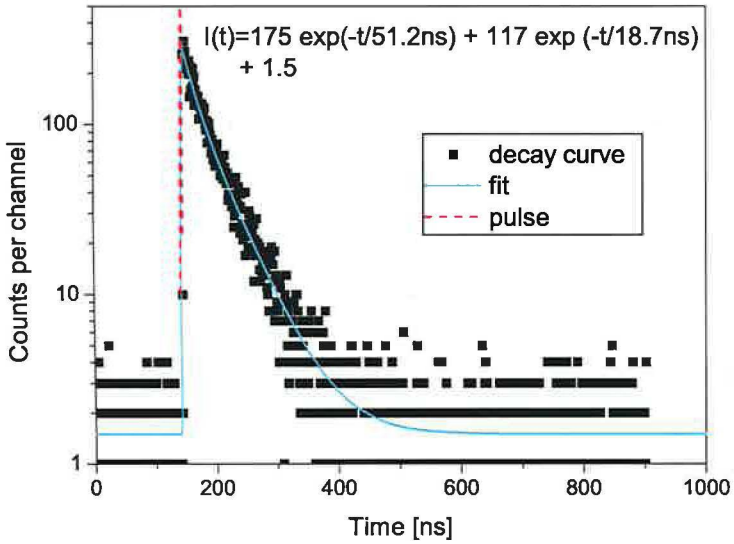

Figure 7.23: Decay curve of 1C2 (λ_{ex}=340 nm, λ_{em}=530 nm) at room temperature.

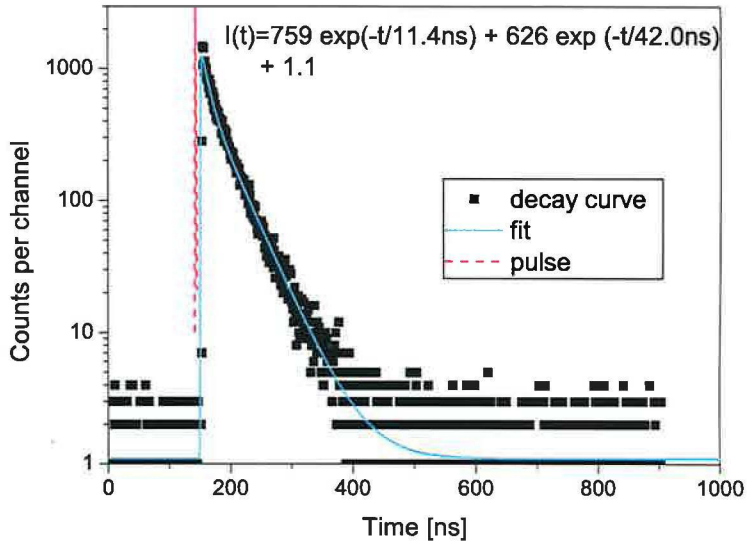

Figure 7.24: Decay curve of 1C3 (λ_{ex}=340 nm, λ_{em}=530 nm) at room temperature.

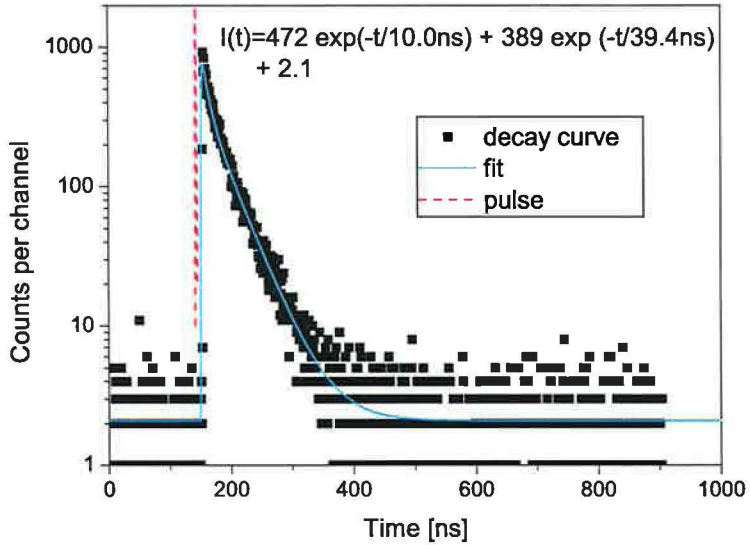

Figure 7.25: Decay curve of 1C5 (λ_{ex}=340 nm, λ_{em}=530 nm) at room temperature.

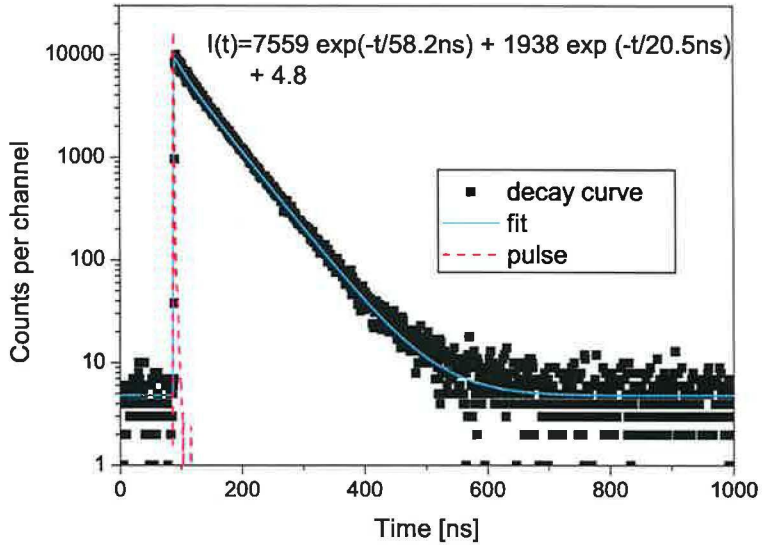

Figure 7.26: Decay curve of 5C2 (λ_{ex}=340 nm, λ_{em}=530 nm) at room temperature.

7.1.2 Optical properties of the samples prepared from the BaO-BaF_2-B_2O_3 flux

The Ce:YAG thin films on pure YAG substrates were grown by LPE from the BaO-based flux. First, the preparation method was established well for undoped YAG layers. Afterwards, two series of the samples doped with cerium 4YBC and 5YBC were grown. The first epitaxial film doped with cerium prepared from the BaO-based flux is 4YBC1. It has a very thin film $d_{4YBC1} = 0.99\mu$m. The samples 5YBC1, 5YBC2, 5YBC3 were successfully prepared from a melt of different ratios of garnet constituents, for thicknesses see Table 7.2. Barium has large atoms. Therefore, it cannot be incorporated into garnet lattice, in which there is not enough space for it. The BaO-based flux does not etch the platinum crucible thus the epitaxial layers do not contain Pt. On the other hand, all epitaxial films prepared from the BaO-based flux have much worse surface quality than layers grown from the PbO-based flux, see Fig. 7.27. This results from high viscosity and high surface tension of this solvent.

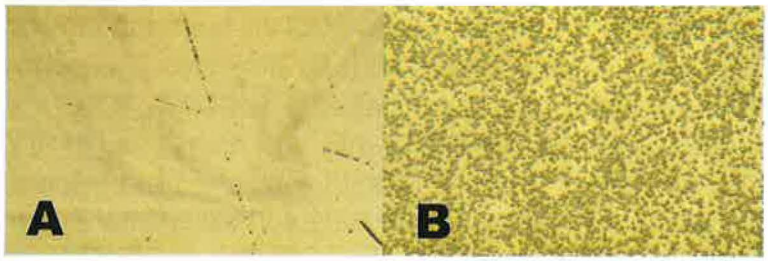

Figure 7.27: Photographs of the surface of samples prepared from the BaO-based flux. **A** is the surface of the sample 5YB1 - YAG layer on YAG substrate. The lines comes from scratches in substrate originating in polishing procedure. **B** is the surface of the sample 5YBC1 - Ce:YAG layer on YAG substrate. The surface is not uniform, with a lot of defects and scatters the light strongly.

Absorption spectra

The absorption coefficient is plotted in Fig. 7.28. The absorption spectra are typical for Ce^{3+} doped in YAG. The increasing absorption below 280 nm (above 5 eV), which is a typical feature in the absorption spectra of the 1C - 5C series, is considerably lower here. The shape of the spectra is much more similar to Ce:YAG single crystal, see Fig. 7.47. They also show almost zero absorption in the spectral range between 3 eV and 3.5 eV compared to layers grown from the PbO-based flux. The 5YBC series has the highest concentration of cerium, Table 7.2.

Luminescent spectra

Luminescent spectra, both excitation and emission, are typical for Ce^{3+} doped in YAG garnet. Layers prepared from the BaO-based flux exhibit higher luminescence intensity, at least by one order of magnitude compared to samples grown from the PbO-based flux, Figs. 7.29-7.31. In excitation spectra Fig. 7.29, it is possible to observe the third band at 230 nm corresponding to the transition in the Ce^{3+} ion, Fig. 4.4, Fig. 7.48. The highest intensity of emission was measured for 5YBC2. It has the greatest thickness, Table 7.2. The lowest light

output has 4YBC1, because of its low thickness. The feature between 400 nm and 450 nm originating probably in impurities, commonly present in the emission spectra of the 1C - 4C series, is weakly visible too, Fig. 7.31. However, its intensity is about three orders of magnitude lower than the emission maximum at λ=530 nm. This is in contrast with 1C - 4C series where the intensity of the emission maximum is of about 1-2 orders stronger than the intensity of the feature.

Kinetics of luminescence

The kinetics of luminescence was measured under the same conditions as with the epitaxial layers prepared from the PbO-based flux. The samples were excited at λ=340 nm and the luminescence was collected at λ=530 nm at room temperature. Decay curves exhibit obviously linear dependence indicating one-exponential decay, Figs. 7.32-7.34. This was confirmed by fitting in the Spectra Solve program. Due to high light emission we succeeded to perform a high quality experiment with a signal to noise ratio greater than 10^3 in the case of kinetics of samples 5YBC1 and 5YBC2. Decay times of samples 5YBC1 (60.2 ns) and 5YBC2 (59.9 ns) correspond very well to the Ce:YAG single crystal, Fig. 7.51. The decay time of the sample 4YBC1 (56.3 ns) is slightly reduced. This can indicate worse sample quality. Sample 4YBC1 has a very thin film and its luminescence intensity is much lower. Therefore, signal to noise ratio is not so high as in the previous experiment and the decay time measurement has a substantially higher inaccuracy.

All decay curves of 5YBC and 4YBC series are one-exponential and differ greatly from layers prepared from the PbO-based flux. Even the purest sample 5C2 has two-exponential decay, Fig. 7.26. As a result in samples grown from the BaO-based flux any energy transfer do not occur and the luminescence is not quench by nonradiative transitions.

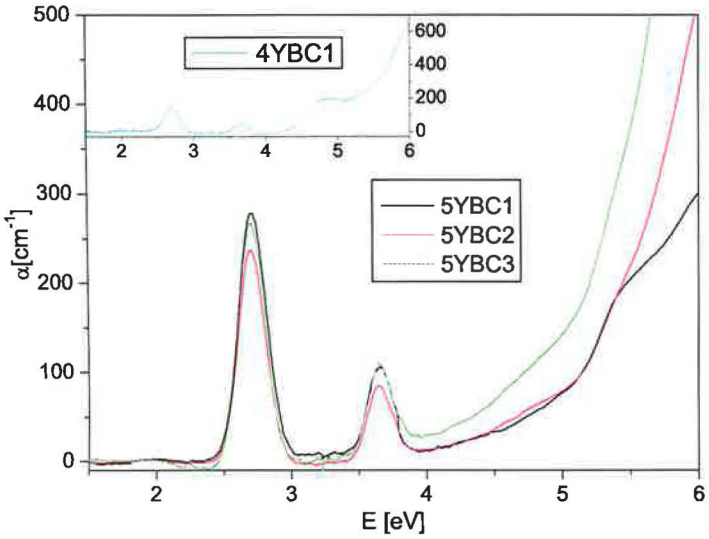

Figure 7.28: Absorption spectra.

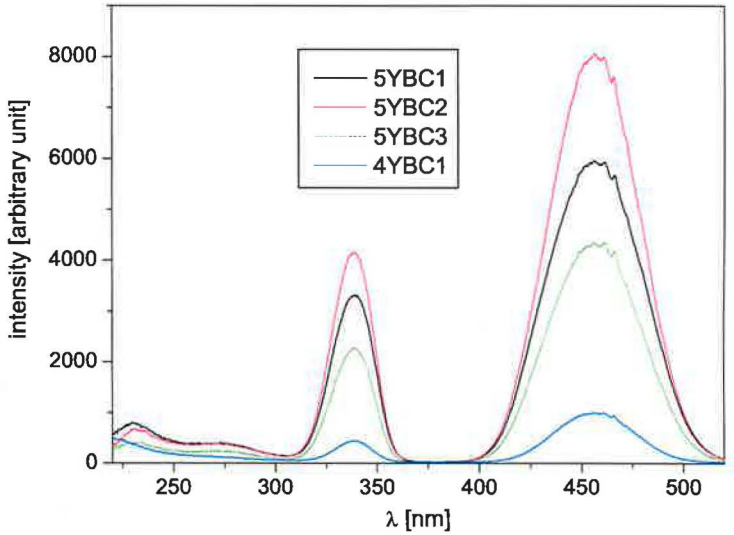

Figure 7.29: Excitation spectra at λ_{em}=550 nm.

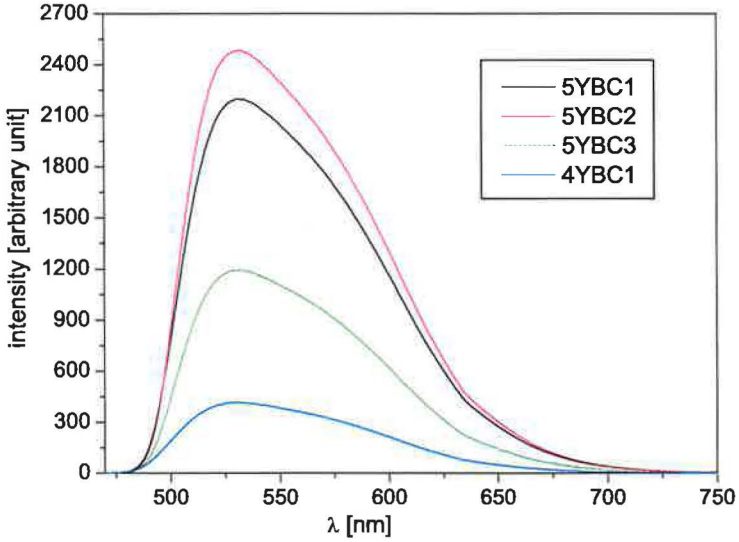

Figure 7.30: Emission spectra at λ_{ex}=455 nm.

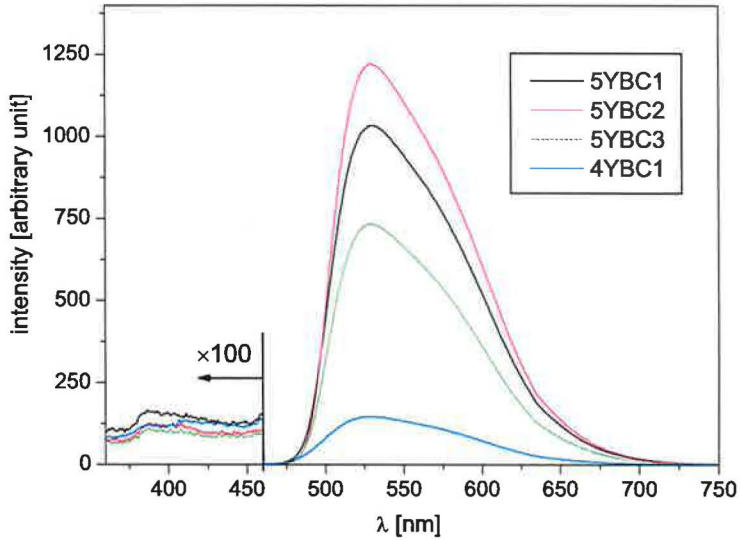

Figure 7.31: Emission spectra at λ_{ex}=340 nm.

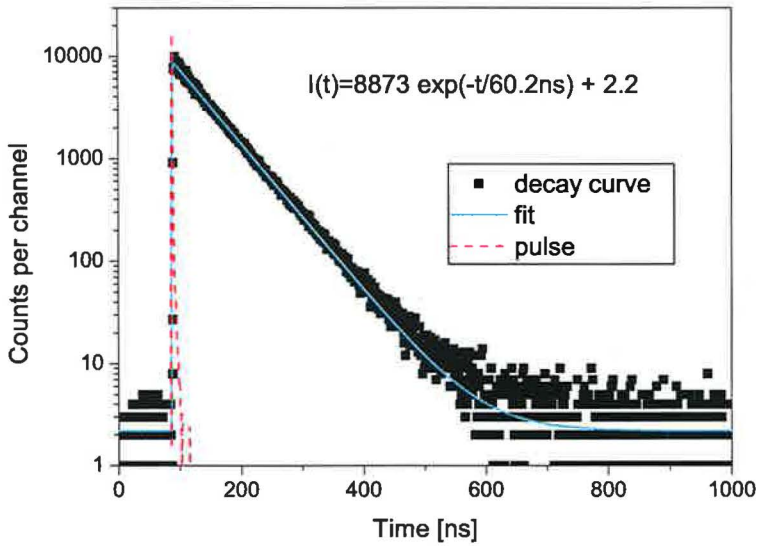

Figure 7.32: Decay curve of 5YBC1 (λ_{ex}=340 nm, λ_{em}=530 nm) at room temperature.

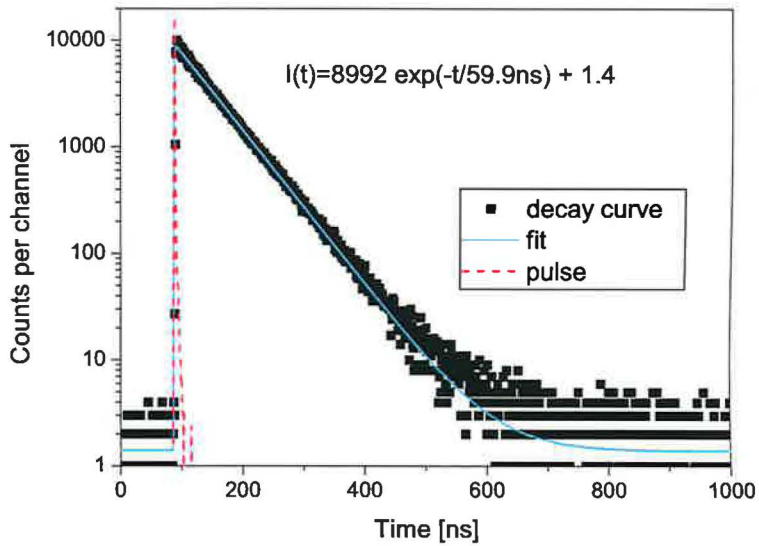

Figure 7.33: Decay curve of 5YBC2 (λ_{ex}=340 nm, λ_{em}=530 nm) at room temperature.

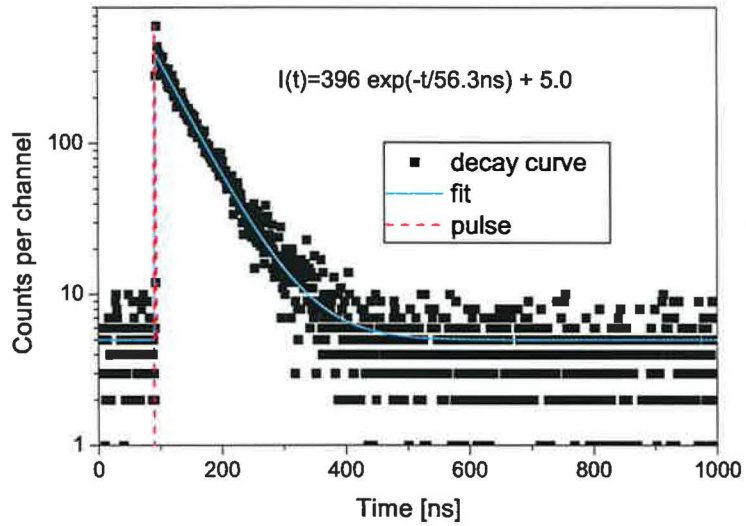

Figure 7.34: Decay curve of 4YBC1 (λ_{ex}=340 nm, λ_{em}=530 nm) at room temperature.

7.2 Optical properties of Ce:LuAG thin films

Ce:LuAG epitaxial films were prepared on pure LuAG substrates by LPE from the BaO-BaF_2-B_2O_3 flux. We succeeded in growing two samples 1LC1 and 1LC2 with thickness less than 2 μm, Table 7.2. Their surface is not homogenous and scatters the light strongly, Fig. 7.35, as is typical for the layers prepared from the BaO-based flux.

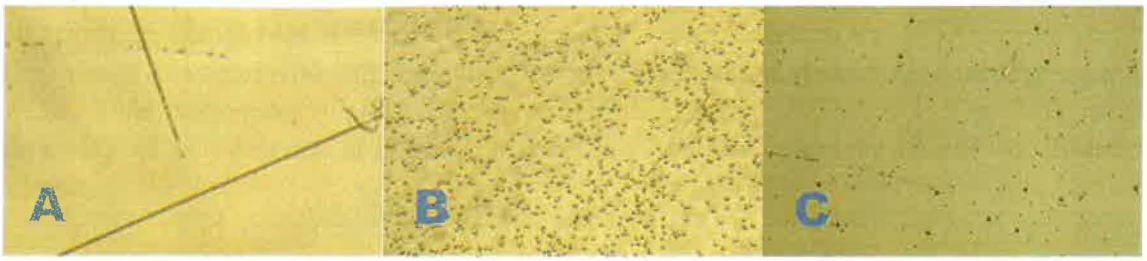

Figure 7.35: Photographs of the surface of Ce:LuAG thin films prepared from the BaO-based flux. **A** is the surface of the sample 1L2 - LuAG layer on LuAG substrate, Table 7.3. It has the smooth surface. The lines comes from scratches in the substrate originating in the polishing procedure. **B** is the surface of the sample 1LC1 - Ce:LuAG layer on LuAG substrate. The surface is not uniform, with a lot of defects and scatters the light strongly. **C** is the surface of the sample 1LC2 - Ce:LuAG layer on LuAG substrate. The surface has much better quality than in the case of the sample 1LC1. There are only a few defects.

Absorption spectra

Absorption spectra were measured under the same conditions as with all previous samples. The absorption coefficient is plotted in Fig. 7.36. The spectra have a characteristic shape which corresponds to Ce^{3+} doped into garnet matrix. The absorption maxima are observed at λ=448 nm, 346 nm (2.77 eV, 3.58 eV). The peaks are shifted compared to Ce:YAG, Fig. 7.40, where the maxima occur at λ=458 nm, 340 nm (2.70 eV, 3.65 eV). The 1LC series shows almost zero absorption between 3 eV and 3.4 eV as Ce:YAG prepared from the BaO-based flux. The absorption above 5 eV rises steeply in comparison with the 5YBC and 4YBC series. Ce:LuAG likely contains more impurities originating from the purity of raw materials. Probably Lu_2O_3 applied for preparation was not pure enough compared to Y_2O_3. The broad peak around 255 nm (4.9 eV) is also observed in the absorption spectra of LuAG and YAG epitaxial films, Fig. 7.41. It seems to be probably connected with some impurity included in substrates.

Luminescent spectra

The luminescent spectra were measured in the same experimental setup as the other samples and exhibit typical features of Ce^{3+} doped into garnet lattice. The excitation spectra show a high level of noise, Fig. 7.37. The intensity of luminescence was low. The sample 1LC2 has a higher light output. It is slightly thicker than the sample 1LC1, Table 7.2. Afterwards, the samples were excited at λ=345 nm and at λ=445 nm corresponding to the maxima in their excitation spectra. The emission spectra are plotted in Figs. 7.38, 7.39. Maximum emission occurs at λ=500 nm.

In comparison with Ce:YAG layers prepared from the BaO-based flux, Ce:LuAG exhibits a luminescence intensity lower by about two orders of magnitude. Ce:LuAG epitaxial layers contain the highest cerium concentration of all samples, but they are very thin, Table 7.2. The positions of spectral bands in the excitation spectra of Ce:YAG are different (λ=340 nm, 455 nm). The maximum of cerium emission for Ce:LuAG is shifted to shorter wavelengths (λ=500 nm) compared to Ce:YAG (λ=530 nm), Fig. 7.40. This is due to different composition of the garnet matrix. The colours of cerium emission can be affected due to various substitutions in the garnet lattice, Robertson et al. [30], Zorenko et al. [13]. The feature in spectral range between 400 nm and 450 nm in the emission spectra is missing completely, Fig. 7.39. This corresponds well with the emission spectra of Ce:YAG, Fig. 7.31, in which the intensity of the feature is negligible compared to the intensity of cerium emission at λ=530 nm.

Kinetics of luminescence

The kinetics of luminescence was measured under the same conditions as with Ce:YAG prepared from the BaO-based flux. Ce:LuAG epitaxial layers were excited at λ =340 nm and emission was registered for λ =530 nm at room temperature. Deconvolution was done in the same way. In contrast to Ce:YAG grown from the BaO-based flux the decay curves were fitted by two-exponential decay, Figs. 7.42, 7.43. We tried to estimate the influence of the fast component as it was done in Subsection 7.1.1. The quantum efficiency of the luminescence is decreased due to nonradiative transitions of about 4% and 3% in the samples 1LC1 and 1LC2 respectively. The sample 1LC1 is significantly distorted from the ideal decay curve. It has decay time 61 ns. The decay time for Ce:LuAG is 54 ns at room temperature, Table 4.1. This may be caused due to worse surface quality, Fig. 7.35. The sample 1LC2 has much better decay characteristics. However, the perturbation of an ideal one-exponential decay is great. The fast component has an amplitude comparable to the slower component. We suppose that higher concentration of some quench centres may be present in samples 1LC1 and 1LC2 compared to Ce:YAG epitaxial films.

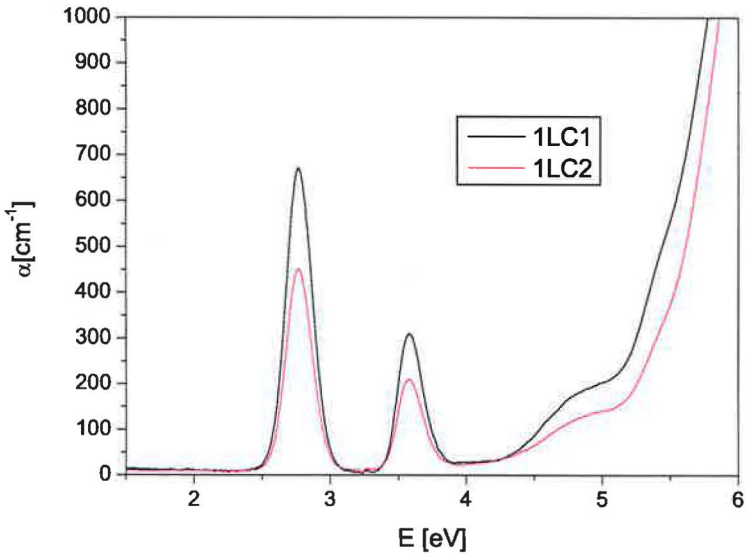

Figure 7.36: Absorption spectra.

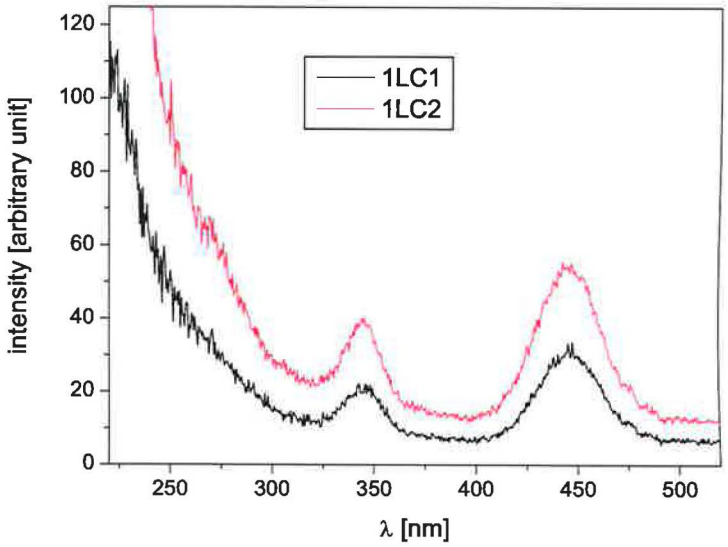

Figure 7.37: Excitation spectra at λ_{em}=550 nm.

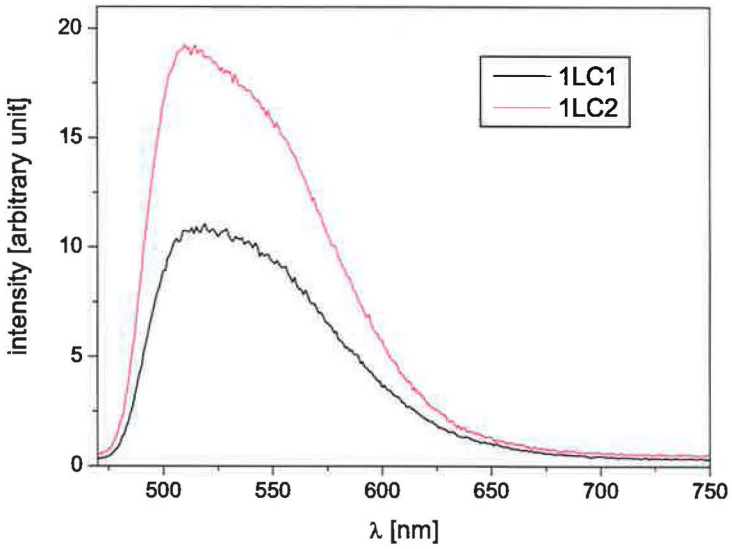

Figure 7.38: Emission spectra at λ_{ex}=445 nm.

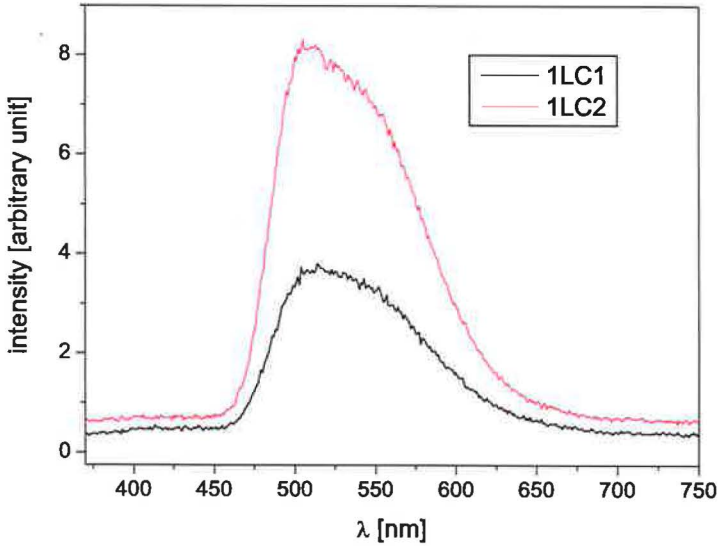

Figure 7.39: Emission spectra at λ_{ex}=345 nm.

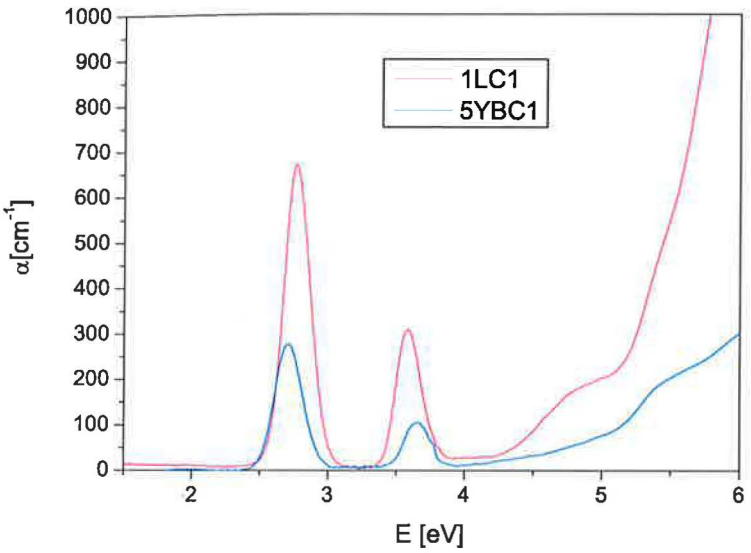

Figure 7.40: Absorption spectra of Ce:YAG (5YBC1) and Ce:LuAG (1LC1) epitaxial films prepared from the BaO-based flux on YAG and LuAG substrates, respectively.

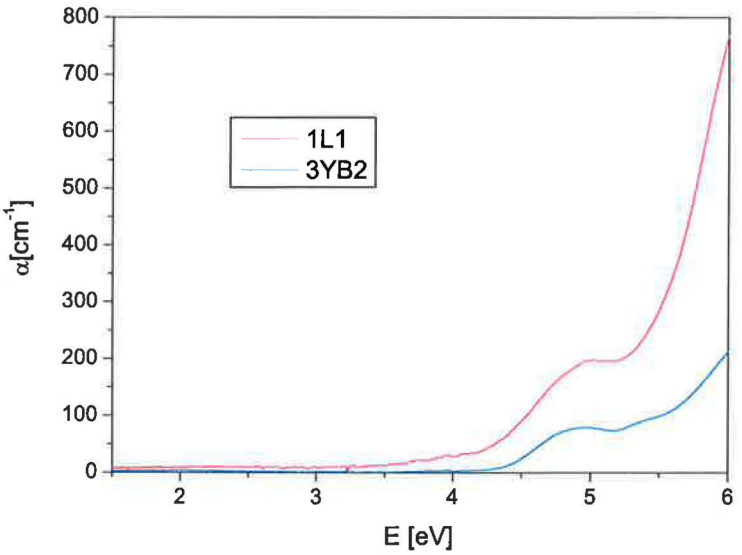

Figure 7.41: Absorption spectra of YAG (3YB2) and LuAG (1L1) epitaxial films prepared from the BaO-based flux on YAG and LuAG substrates, respectively, for thicknesses see Table 7.3.

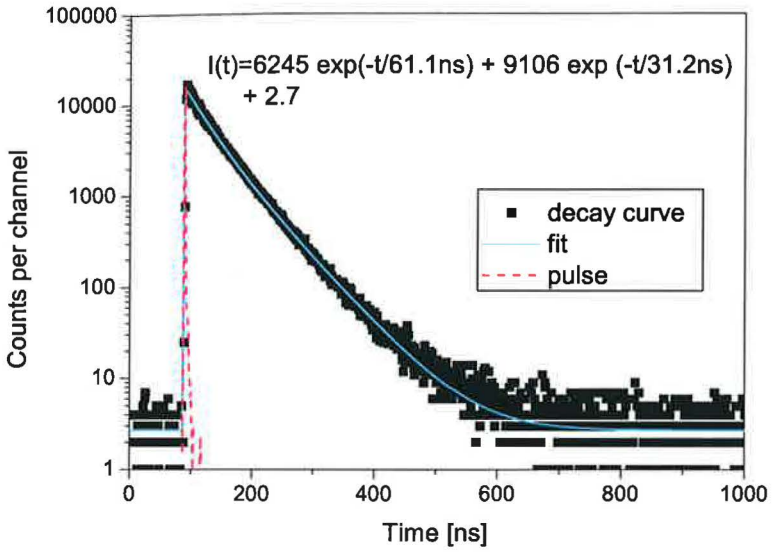

Figure 7.42: Decay curve of 1LC1 (λ_{ex}=340 nm, λ_{em}=530 nm) at room temperature.

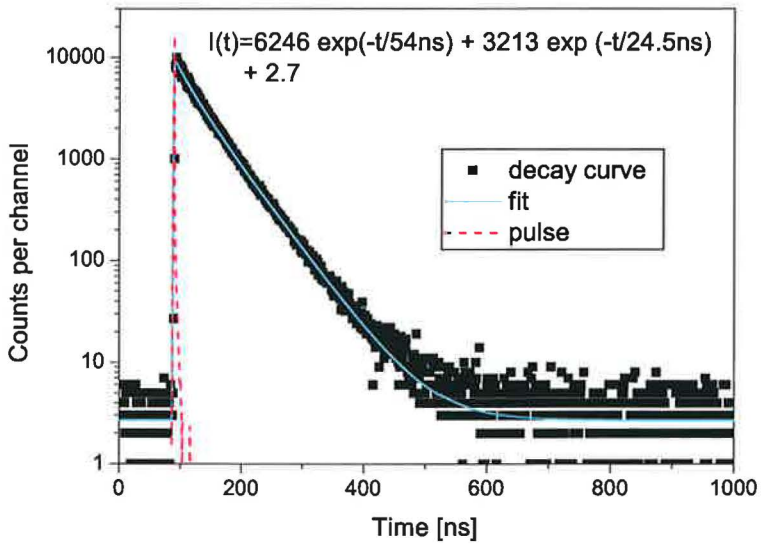

Figure 7.43: Decay curve of 1LC2 (λ_{ex}=340 nm, λ_{em}=530 nm) at room temperature.

7.3 Impurities

In the previous sections, the optical spectra of Ce:YAG and Ce:LuAG thin films were discussed. The results show that impurities are present in the epitaxial layers. These impurities originate from the melt, since the raw materials are not pure enough. PbO used for the preparation of the 1C - 4C series contains high concentration of Fe impurity, Table 7.1. Especially Fe and Mn may influence optical properties. Pb from the flux and Pt coming from the platinum crucible absorb in the spectral range above 4.75 eV (~260 nm), which overlaps with the absorption band of Ce^{3+} at 5.3 eV (~230 nm).

In order to obtain more information, the luminescence spectra were measured on three types of the samples: Ce:YAG thin films prepared from the PbO-based flux (4C4) and from the BaO-based flux (4YBC1) and pure YAG substrate without layer (1C1). First, the emission spectra were recorded at λ_{ex}=256 nm, Fig. 7.44. That corresponds to the observed shoulder in the absorption spectra, Fig. 7.46. A strong luminescent peak extending around 800 nm was found, Fig. 7.44. This feature is observed not only in the emission spectra of thin films 4C4 prepared from the PbO-based flux and 4YBC1 prepared from the BaO-based flux but also in the emission spectrum of YAG substrate without layer (1C1). Unfortunately, when samples are excited at λ_{ex}=256 nm, the light goes through the layer in to the substrate. Hence, the contributions from substrate and from the layer could not be separated. This peak at 800 nm is characteristic for Fe^{3+} impurity in YAG, Rotman et al. [31], [32].

The broad luminescent band around 550 nm in the spectra of the samples 4C4 prepared from the PbO-based flux and 4YBC1 prepared from the BaO-based flux is the cerium emission, Fig. 7.44. Ce:YAG single crystal has very broad absorption band at λ=230 nm, Fig. 7.47, which consits of three constituents, see Table 4.2. Hence, Ce^{3+} is also excited. Also some energy transfer may occur due to the fact that the energy levels of Ce^{3+} and Fe^{3+} ions are close to each other.

Origin of the broad band with a maximum at 400 nm in the emission spectrum of the sample 4YBC1 grown from the BaO-based flux is unknown,Fig. 7.44. Probably it may relate to the surface quality of this sample.

Furthermore, the excitation spectra of these three kinds of samples were registered, Fig. 7.45. The emission was collected at λ_{em}=780 nm which corresponds to Fe^{3+} emission. The spectrum of the sample 4YBC1 prepared from the BaO-based flux has a shape similar to the spectrum of YAG substrate (1C1). In all three samples, a peak at 256 nm originating from Fe^{3+} is present. The peak observed at λ=220 nm is missing in the spectrum of the sample 4C4 prepared from the PbO-based flux probably because it absorbs strongly in this spectral range.

The excitation and emission spectra in Figs. 7.44, 7.45 are typical for Fe impurity in YAG. Fe absorbs at λ=256 nm and emits light at λ=800 nm. Everything indicates that YAG substrates contain some concentration of iron. Fe is also present in high concentration (~400ppm) in the PbO, from which the 1C - 4C series were prepared, Table 7.1.

The influence of impurities originating from the melt and incorporated in the epitaxial layers is demonstrated in Fig. 7.46. The absorption spectra of YAG crystal and YAG thin film 5C1 prepared from the PbO-based flux on YAG substrate are compared. The basic difference is the rising absorption in the spectral range above 5 eV for sample 5C1. YAG crystal also contains some impurity, which absorbs around 4.75 eV (~260 nm). Probably it may be Fe, as is discussed above. High purity YAG crystals are transparent up to 7 eV, Tomiki [18].

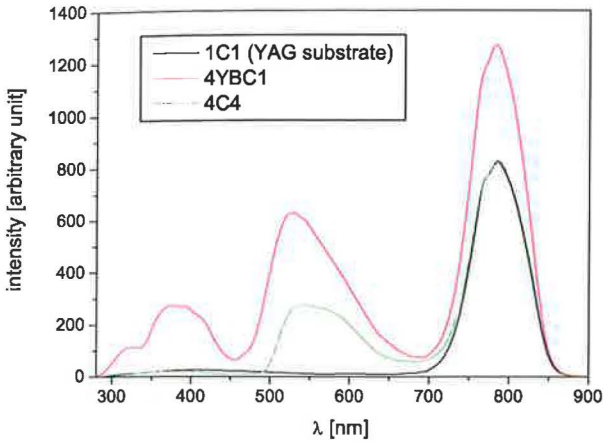

Figure 7.44: Emission spectra of pure YAG substrate (1C1) and Ce:YAG epitaxial layers prepared from the PbO-based flux (4C4) and the BaO-based flux (4YBC1), samples were excited at λ=256 nm.

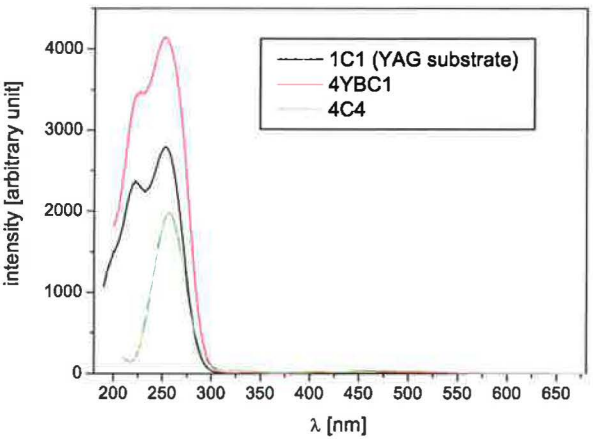

Figure 7.45: Excitation spectra of pure YAG substrate (1C1) and Ce:YAG epitaxial layers prepared from the PbO-based flux (4C4) and the BaO-based flux (4YBC1), the emission was collected at λ=780 nm.

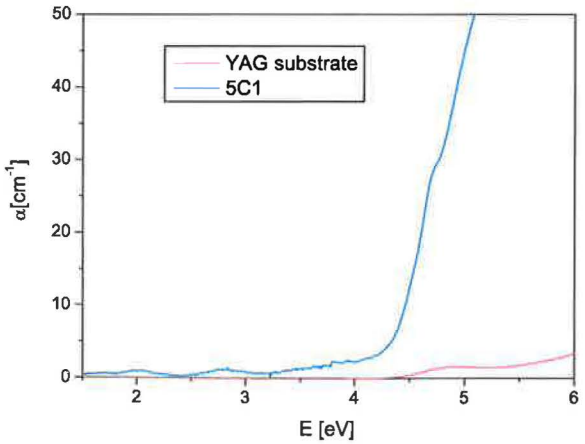

Figure 7.46: Absorption spectra of pure YAG substrate and YAG epitaxial layer prepared from the PbO-based flux on YAG substrate (5C1), for thickness see Table 7.3.

7.4 Comparison of Ce:YAG single crystal, Ce:YAG epitaxial layers prepared from the PbO-based and the BaO-based fluxes

The optical spectra of Ce:YAG epitaxial films discussed above show some differences which originate from impurities and applied melt composition. Samples prepared under different conditions are compared in Figs. 7.47-7.50. 4C1 is the epitaxial layer of Ce:YAG prepared by LPE from the PbO-based flux. 5C2 was also grown from the PbO-based flux, but is prepared from a flux of much higher purity than the 1C - 4C series. 5YBC1 is a thin film prepared from the BaO-based flux. To compare Ce:YAG single crystal grown by Czochralski method is also displayed in Figs. 7.47-7.50.

The absorption spectra show a lot of differences, Fig. 7.47. Ce:YAG single crystal is of the highest purity. Hence, it exhibits the ideal absorption spectrum. Three peaks are observed at 2.7 eV, 3.6 eV and 5.3 eV, corresponding to transitions among the levels of the Ce^{3+} ion in YAG matrix, Fig. 4.4. Samples 4C1, 5C2 and 5YBC1 show two low energy peaks at 2.7 eV, 3.6 eV, Fig. 7.47. However, the shapes of spectra differ extremely in the range above 5 eV. The samples prepared from the PbO-based flux have a steeply rising absorption. This absorption results from Pb, and Pt impurities and in the case of the sample 4C1 also from Fe impurities, Section 7.3, and other unidentifiable impurities, which overlap the cerium emission at 5.3 eV. On the other hand, the absorption coefficient of the sample 5YBC1 prepared from the BaO-based flux is much lower in this spectral range. However, it increases as well, likely due to unidentifiable impurities in raw materials. The sample 5YBC1 has the highest concentration of cerium, Table 7.2, as it has the highest absorption coefficient at 2.7 eV, Fig. 7.47.

The measurements of luminescence spectra were made using different slits. The samples have different thicknesses, shapes, and Ce concentrations. They cannot be compared directly. The excitation spectra are plotted in Fig. 7.48. The spectrum of Ce:YAG single crystal has three peaks at wavelengths 455 nm, 340 nm, and 230 nm. It has the highest luminescence intensity because of its 100× highest thickness. The structure of the maximum at 455 nm arises probably from experimental equipment. Among the epitaxial layers, sample 5YBC1, which was prepared from the BaO-based flux, has the highest light output. The samples 4C1 and 5C2 prepared from the PbO-based flux have much lower intensities. The emission spectra of all four samples have a typical shape of a broad band with a maximum at λ=550 nm composed of two components, Figs. 7.49, 7.50.

The decay curve of the Ce:YAG single crystal exhibits one-exponential decay, Fig. 7.51. The decay time is 63 ns. On the other hand, in samples prepared from the PbO-based flux, the decrease in quantum efficiency of luminescent centres at Figs. 7.23-7.26 is apparent and the decay is two-exponential. Both fast and slow components have similar amplitudes in samples prepared from the PbO-based flux. Samples grown from the BaO-based flux provide much better kinetics of luminescence, exhibiting an almost ideal one-exponential decay, Fig. 7.32-7.34. In contrast to Ce:YAG single crystal they have only a slightly lower decay time.

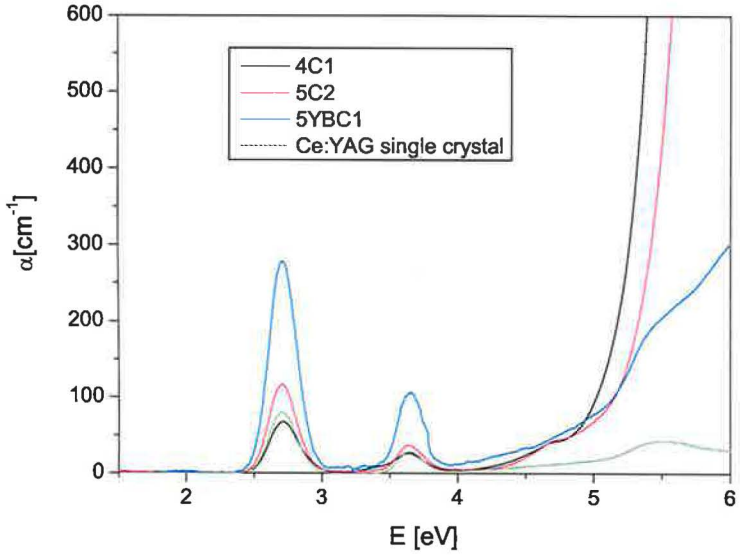

Figure 7.47: Absorption spectra.

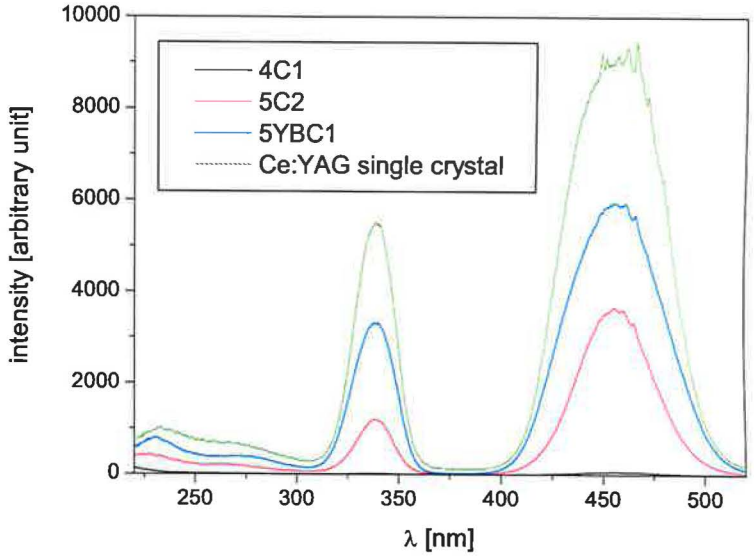

Figure 7.48: Excitation spectra at λ_{em}=550 nm.

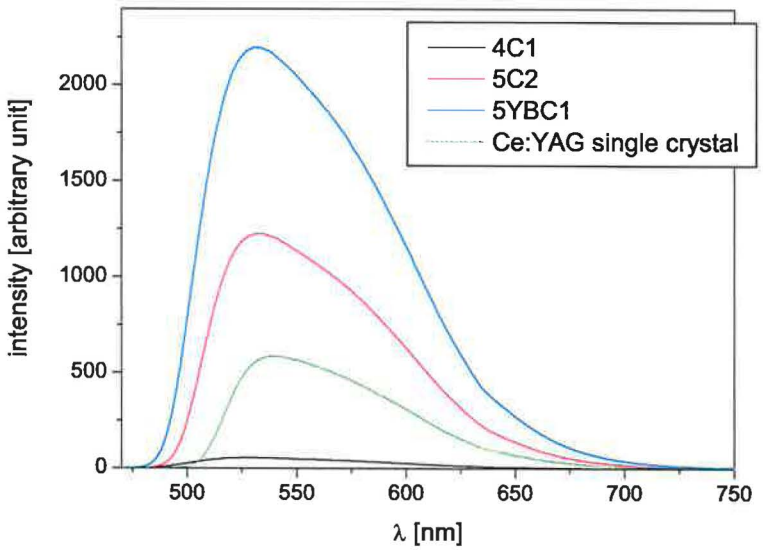

Figure 7.49: Emission spectra at λ_{ex}=455 nm.

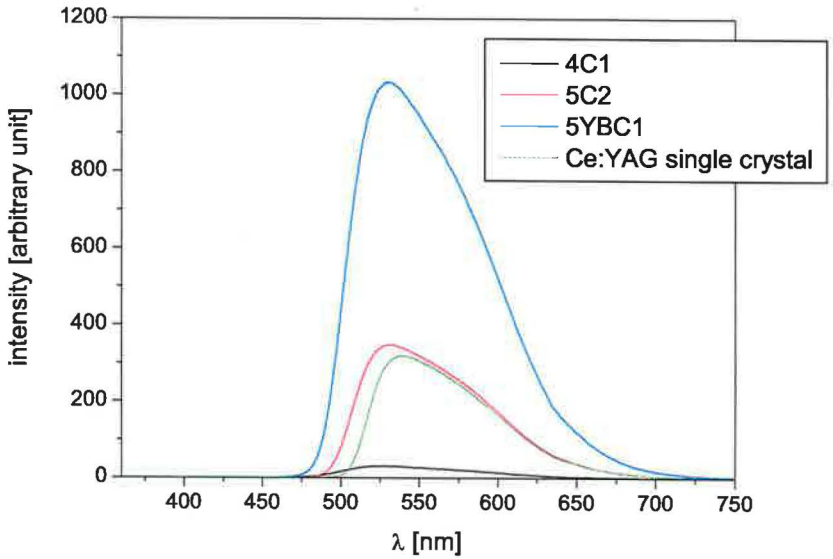

Figure 7.50: Emission spectra at λ_{ex}=340 nm.

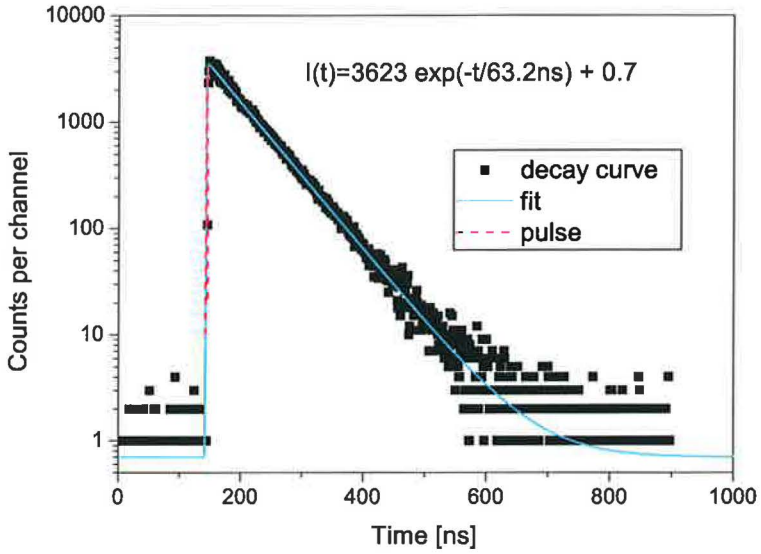

Figure 7.51: Decay curve of Czochralski grown Ce:YAG single crystal (λ_{ex}=340 nm, λ_{em}=530 nm) at room temperature.

Chapter 8

Conclusion

In this Diploma Thesis, the influence of melt composition and growth conditions on crystallographic, optical, emission, and kinetic properties of cerium doped yttrium aluminum garnet (Ce:YAG) epitaxial films prepared by liquid phase epitaxy (LPE) on YAG substrates was investigated. YAG, LuAG (lutetium aluminum garnet), Ce:YAG, Ce:LuAG epitaxial layers were successfully prepared by the LPE method at growth temperatures ranging from 920°C to 1042°C. 32 samples were grown from melts of different compositions and at different growth conditions. They have thicknesses in range 1-25 μm. Absorption, excitation, and emission spectra and kinetic of luminescence were measured. All thin films exhibit intense green-yellow luminescence. In the absorption spectra of Ce^{3+} doped layers, two broad peaks at 458 nm (2.7 eV) and 340 nm (3.6 eV) were observed corresponding to $4f \rightarrow 5d$ transitions of Ce^{3+} ion in the garnet lattice. The epitaxial films were prepared from melts containing two different fluxes: the PbO-B_2O_3 flux and the BaO-BaF_2-B_2O_3 flux. The PbO-based flux is volatile and reacts with the platinum crucible. The BaO-based flux is a nonvolatile, nontoxic solvent, with negligible reactivity with the platinum crucible. However, it has a high viscosity.

Epitaxial films grown from the $PbO - B_2O_3$ flux have the following characteristics:

- All samples exhibit excellent crystallographic properties. X-ray diffraction confirmed that the surface of all films displays high optical quality.
- Optical spectra show that some impurities were incorporated into the layers. Steeply rising absorption in the ultraviolet region below 280 nm originates from Pb, Pt, and Fe impurities.
- The concentration of cerium (x=0.008-0.043) and impurities in films increases with supercooling and with decreasing growth temperature.
- From the luminescence spectra it follows that impurities partly quench the luminescence and are also responsible for two-exponential decay in kinetic measurements. The fast component distorts the ideal decay curve.
- The results indicates that it is necessary to use pure raw materials of at least 5N purity in technological experiments. Critical impurities (Fe) which quench the luminescence have to be eliminated $\leq$1 ppm.

Epitaxial layers prepared from the $BaO - BaF_2 - B_2O_3$ flux exhibit the following properties:

- The growth of epitaxial layers is much more complicated than from the PbO-based flux. High viscosity of this solvent - of about two orders of magnitude higher than of the PbO-based flux at 1000°C - implies that the growth of layers is more difficult and the layers display worse crystal and surface quality.
- On the other hand, thin films do not contain Pb and Pt impurities. The concentration of impurities in films depends only on the purity of raw materials. Ba atoms do not enter into the garnet lattice because of their large radius.
- Epitaxial films prepared from the BaO-based flux exhibit better purity and much higher light yield than layers grown from the PbO-based flux.
- It was found that it is possible to prepare epitaxial layers from the BaO-based flux with a higher concentration of cerium (x=0.037-0.070) than from the PbO-based flux.
- Absorption in the UV region is much lower due to low concentrations of impurities.
- The decay curves are one-exponential and the luminescence is not quenched by nonradiative transitions into traps.

In summary, the PbO-based flux provided worse optical properties of the layers due to the inevitable occurrence of impurity ions. While the BaO-based flux afforded films with substantially better luminescence properties, however, the films had worse surface quality with lots of defects due to the high viscosity of this solvent. For practical applications, the problem with high viscosity of the solvent should be solved. The quality of the surface also depends on the quality of the substrate, which must not contain dislocations, inclusions, etc., and on the method of preparation of the surface of the substrate for LPE.

It was demonstrated that LPE method is perspective for the preparation of thin films of scintillator materials and its development will continue.

Bibliography

[1] Nikl M.: *Výsledky a trendy ve výzkumu scintilačních materiálů*, Československý časopis pro fyziku, **54** (2004), 66-76.

[2] Nikl M.: *Anorganické scintilátory - k čemu mohou sloužit?*, Československý časopis pro fyziku, **55** (2005), 347-349.

[3] Nikl M.: *Scnitilltion detectors for x-rays*, Measurement Science and Technology, **17** (2006), R37-R54.

[4] van Eijk C.W.E: *Inorganic scintillator in medical imaging*, Physics in Medicine and Biology **47** (2002), R85-R106.

[5] Zorenko Yu., Gorbenko V., Konstankevych I., Grinev B., Globus M., Batentschuk M.: *Application of scintillators based on sinle-crystalline* $Lu_3Al_5O_{12} : Ce^{3+}$ *films for radiation monitoring in biology and medicine*, Semiconductor Physics, Quantum Electronics & Optoelectronics, **3** (2000), 213-218.

[6] Zorenko Yu., Konstankevych I., Globus M., Grinyov B., Lyubinskiy V.: *New scintillation detectors based on oxide single crystal films for biological microtomography*, Nuclear Instruments and Methods in Physics Research, **A 505** (2003), 93-96.

[7] Nikl M., Mihokova E., Pejchal J., Vedda A., Zorenko Yu., Nejezchleb K.: *The antisite* Lu_{Al} *defect-related trap in* $Lu_3Al_5O_{12} : Ce$ *single crystal*, Physica Status Solidi B, **242** (2005), R119-R121.

[8] Vedda A., Fasoli M., Moretti F., Mihokova E., Nikl M., Pejchal J., Zorenko Yu., Gorbenko V., Blazek K., Nejezchleb K.: *Trap levels and recombination centres in LPE grown Ce-doped LuAG and YAG thin films*, to be published.

[9] Solé J.G., Bausá L.E., Jaque D.: *An introduction to the optical spectroscopy of inorganic solids*, John Wiley & Sons Ltd., Chichester (2005), 17.

[10] Blasse G., Grabmaier B.C.: *Optical properties of solids*, Springer-Verlag, Berlin (1994), 186-203.

[11] Fox M.: *Luminescent materials*, Oxford University Press, New York (2001), 10-32.

[12] Rodnyi A.P.: *Physical processes in inorganic scintillators*, CRC Press, New York (1997), 1-51.

[13] Zorenko Yu., Gorbenko V., Konstankevych I., Grinev B., Globus M.: *Scintillation properties of $Lu_3Al_5O_{12}$: Ce single-crystalline films*, Nuclear Instruments and Methods in Physics Research, **A 486** (2002), 309-314.

[14] van Eijk C.W.E: *Inorganic-scintillator development*, Nuclear instruments and Methods in Physics Research **A 460** (2001), 1-14.

[15] Krupička S.: *Fyzika feritů a příbuzných magnetických kysličníků*, Academia, Praha (1969), 95-99.

[16] Kuwano Y., Suda K., Ishizawa N., Yamada T.: *Crystal growth and properties of $(Lu, Y)_3Al_5O_{12}$*, Journal of Crystal Growth, **260** (2004), 159-165.

[17] Crytur: http://www.crytur.cz.

[18] Tomiki T., Ganaha Y., Shikenbaru T., Futemma T., Yuri M., Aiura Y., Fukutani H., Kato H., Tamashiro J., Miyahara T., Yonesu A.: *Optical spectra of $Y_3Al_5O_{12}$ (YAG) single crystals in the vacuum ultraviolet region. II*, Journal of The Physical Society of Japan, **62** (1993), 1388-1400.

[19] Tomiki T., Akamine H., Gushiken M., Kinjoh Y., Miyazato M., Miyazato T., Toyokawa N., Hiraoka M., Hirata N., Ganaha Y., Futemma T.: *Ce^{3+} centres in $Y_3Al_5O_{12}$ (YAG) single crystals*, Journal of The Physical Society of Japan, **60** (1991), 2437-2445.

[20] Robbins D.J.: *The effects of crystal field and temperature on the photoluminescence excitation efficiency of Ce^{3+} in YAG*, Journal of Electrochemical Society, **126** (1979), 1550-1555.

[21] Robertson J.M., van Tol M.W., Heynen J.P.H., Smits W.H., De Boer T.: *Thin single crystalline phosphor layers grown by liquid phase epitaxy*, Philips Journal of Research, **35** (1980), 354-371.

[22] Zorenko Yu., Gorbenko V., Voloshinovskii A., Stryganyuk G., Mikhailin V., Kolobanov V., Spassky D., Nikl M., Blazek K.: *Exciton-related luminescence in LuAG:Ce single crystals and single crystalline films*, Physica Status Solidi, **A 202** (2005), 1113-1119.

[23] Zorenko Yu., Gorbenko V., Konstankevych I., Voloshinovskii A., Stryganyuk G., Mikhailin V., Kolobanov V., Spassky D.: *Single-crystalline films of Ce-doped YAG and LuAG phospors: advantages over bulk crystals analogues*, Journal of Luminescence, **114** (2005), 85-94.

[24] Zorenko Yu., Gorbenko V., Mihokova E., Nikl M., Nejezchleb K., Vedda A., Kolobanov V., Spassky D.: *Single crystalline film scintillators based on Ce- and Pr-doped aluminium garnets*, in press.

[25] Winkler G.: *Magnetic garnets*, Vieweg, Braunschweig, Wiesbaden (1981), 448-491.

[26] Robertson J.M., van Tol M.W.: *Cathodoluminescent garnet layers*, Thin Solid Films, Electronics and optics, **114** (1984), 221-240.

[27] Mares J.A., Beitlerova A., Nikl M., Solovieva N., Nitsch K., Kucera M., Kubova M., Zorenko Yu.: *Scintillation and optical propeties of YAG:Ce films grown by Liquid Phase Epitaxy*, in press.

[28] Bond W.L.: *Measurement of the refractive indices of several crystals*, Journal of Applied Physics, **36**, (1965), 1674-1677.

[29] Babin V., Gorbenko V., Makhov A., Mares J.A., Nikl M., Zazubovich S., Zorenko Yu.: *Luminescence characteristics of* Pb^{2+} *centers in undoped and* Ce^{3+}*-doped* $Lu_3Al_5O_{12}$ *single crystalline films and* $Pb^{2+} \rightarrow Ce^{3+}$ *energy transfer processes*, to be published.

[30] Robertson J.M., van Tol M.W., Smits W.H., Heynen J.P.H.: *Colourshift of the* Ce^{3+} *emission in monocrystalline epitaxially grown garnet layers*, Philips Joural of Research, **36** (1981), 15-30.

[31] Rotman S.R., Warde C., Tuller H.L., Haggerty J., *Defect-property correlations in garnet crystals. V. Energy transfer in luminescent yttrium aluminum-yttrium iron garnet solid solutions*, Journal of Applied Physics, **66** (1989), 3207-3210.

[32] Rotman S.R.: *Crystal-field splitting of* Ce^{3+} *5d levels in yttrium aluminum garnet*, Physica Status Solidi, **A 132** (1992), K61-K63.